

# Neutron transport criticality calculations using a parallel monolithic multilevel Schwarz preconditioner together with a nonlinear diffusion acceleration method

Fande Kong<sup>a,\*</sup>

<sup>a</sup>*Computational Frameworks, Idaho National Laboratory, P.O. Box 1625, Idaho Falls, ID 83415-3840*

---

## Abstract

The multigroup neutron transport criticality calculations using modern supercomputers have been widely employed in a nuclear reactor analysis for studying whether or not a system is self-sustaining. However, the design and development of efficient parallel algorithms for the transport criticality calculations is challenging especially when the number of processor cores is large and an unstructured mesh is adopted. In particular, both the compute time and the memory usage have to be carefully taken into consideration due to the dimensionality of the neutron transport equations. In this paper, we study a monolithic multilevel Schwarz preconditioner for the transport criticality calculations based on a nonlinear diffusion acceleration (NDA) method. In NDA, the multigroup nonlinear diffusion equations are computed using an inexact Jacobian-free Newton method with an initial guess generated from a few inverse power iterations. The computed scalar fluxes and eigenvalue are used to evaluate the fission and scattering terms of the transport equations, and then the nonlinear system of transport equations is simplified to a linear system of equations. The linear systems of equations arising from the discretizations of the nonlinear diffusion equations and the transport equations need to be efficiently solved. We propose a monolithic multilevel Schwarz method that

---

\*Corresponding author  
*Email address:* fande.kong@inl.gov (Fande Kong)

is capable of efficiently handling the systems of linear equations for both the transport system and the diffusion system. However, in the multilevel method, algebraically constructing coarse spaces is expensive and often unscalable. We study a subspace-based coarsening algorithm to address such a challenge by exploring the matrix structures of the transport equations and the nonlinear diffusion equations. We numerically demonstrate that the monolithic multilevel preconditioner with the subspace-based coarsening algorithm is twice as fast as that equipped with an unmodified coarsening approach on thousands of processor cores for an unstructured mesh neutron transport problem with billions of unknowns.

*Keywords:* Multilevel Schwarz preconditioner, nonlinear diffusion acceleration, multigroup neutron transport equations, parallel processing, domain decomposition methods

---

## 1. Introduction

The neutron transport criticality calculations play an important role in a nuclear reactor analysis [1, 2]. A neutron transport system is said to be critical if the rate of fission neutron production just equals to the neutron losses because of absorption and leakage [1]. A generalized eigenvalue problem needs to be calculated for checking the criticality of the nuclear reactor system. The criticality calculations of the neutron transport problems are challenging, and a tremendous amount of computational resources are required because of a high dimensionality; e.g., 1D energy, 2D angle and 3D spatial space. With an advancement of modern supercomputers, the high-resolution simulations of the neutron transport problems become possible [3, 4, 5]. However, for efficiently using supercomputers, a scalable parallel eigenvalue solver need to be designed and developed with taking both the compute time and the memory usage into consideration. In this work, we propose a highly parallel monolithic eigenvalue solver consisting of a nonlinear diffusion acceleration, a Jacobian-free Newton-Krylov method and a multilevel Schwarz preconditioner.

One of the simplest approaches for computing the criticality of the multi-group neutron transport problems is inverse power iteration [1, 6], and the inverse power iteration is still widely used today due to its implementation simplicity. The inverse power iteration is often referred to as “outer iteration”. Sometimes, the inverse power iteration is accelerated with DSA (Diffusion Synthetic Acceleration) [7] or NDA (Nonlinear Diffusion Acceleration) [8, 9]. During each inverse power iteration, an inverse of the streaming-collision operator is required, and the calculation of the operator inverse can be generalized to solve a linear system of equations. Traditionally, a Gauss-Seidel iterative method is employed for solving the linear system of equations group by group where the scattering and the fission terms are computed using the previously updated solution [1, 3]. For each Gauss-Seidel iteration, a within-group subsystem of equations need to be efficiently solved. Two of the most popular approaches for computing the within-group linear system of equations are transport sweeps [4, 5, 10] and multilevel methods [11, 12, 13, 14, 15]. In the current work, we consider multilevel preconditioned iterative Krylov subspace methods that are easy to parallelize and can handle fully irregular meshes and different spatial discretizations. The Krylov subspace methods mostly involve matrix-vector multiplications that can be efficiently implemented and optimized for parallel calculations [16, 17]. In addition, the multilevel preconditioning technique can be carried out in a scalable way based on the domain decomposition methods, and it is employed to accelerate the convergence of the Krylov subspace methods, which will be discussed shortly.

However, the inverse power iteration based algorithm framework may converge slowly when the smallest eigenvalue and the second smallest eigenvalue are close to each other, which is often true for realistic problems. To address this challenge, while there exist other popular schemes such as Wielandt shift [6, 18], we employ an inexact Jacobian-free Newton method [19, 20, 21]. The Newton-based eigenvalue solver has been successfully applied to many applications [11, 12, 21, 22, 23, 24], just name a few. A direct application of the Jacobian-free Newton-based eigenvalue solver to the multigroup neutron

transport equations sometimes could be expensive because the dimensionality of the nonlinear system of equations is high. One of possible strategies to improve the performance is to apply a nonlinear diffusion acceleration (NDA) method [8, 9, 25], where the neutron transport problem is reformulated as a “fixed source” problem by evaluating the scattering and the fission terms using the scalar fluxes and eigenvalue of the diffusion equations. The NDA method was originally proposed in [8], and its basic idea is directly related to the coarse mesh finite difference method investigated in [26]. The NDA method combined with multigrid in energy was recently studied in [27, 28].

One of the most challenging tasks in the NDA method is to develop a robust and efficient preconditioner for both the transport system and the diffusion system because the transport system is large and the diffusion system is nonsymmetric due to the closure terms. In this work, we study a parallel monolithic multilevel preconditioner together with a subspace-based coarsening algorithm for both the transport system and the diffusion system. More precisely, an inexact Jacobian-free Newton method with an initial guess generated from a few inverse power iterations is employed for the nonlinear diffusion system, and during each Newton iteration the Jacobian system is calculated using the monolithic multilevel Schwarz preconditioner together with GMRES, where unlike a Gauss-Seidel type approach the monolithic method handles all energy groups simultaneously. The transport system is reformed as a fixed source problem under the NDA context, and a linear system of transport equations is also solved using the monolithic multilevel preconditioner together with GMRES. Note, there are other possibilities to explore the basic idea of multilevel methods; e.g., the multilevel methods in energy were studied in [27, 28, 29]; the multilevel methods were constructed in both spatial space and energy [30, 31]. We consider only the algebraic spatial version of the multilevel methods in the current study.

In the multilevel methods, the construction of coarse spaces has a critical impact on the preconditioner performance. In general, a coarse space can be constructed either geometrically [32, 33] or algebraically [24]. We choose to use

an algebraic coarsening algorithm in this work because it is general and has an out-of-box nature for end-users. But it is well-known that the construction of coarse spaces is expensive in terms of the compute time and the memory usage [34], and for some applications the setup phase may be even more expensive than the solve phase. To overcome this difficulty, we introduce a subspace-based coarsening algorithm by exploring the structures of the preconditioning matrices. In the subspace-based coarsening algorithm, only a submatrix needs to be coarsened to generate coarse spaces, and therefore it is able to reduce the computational cost in time and in memory. The subspace-based coarsening was successfully applied to the unaccelerated neutron transport calculations in our previous work [11, 12], and it is improved and extended to solve both the nonlinear diffusion system and the accelerated transport system in the current study. We numerically demonstrate that the proposed algorithm is more efficient than the unmodified traditional multilevel methods for solving both the accelerated transport system and the diffusion system with thousands of processor cores for a 3D unstructured mesh problem with billions of unknowns.

The rest of this paper is organized as follows. In Section 2, a nonlinear diffusion acceleration method is presented to decouple the scattering term and the fission term from the streaming-collision operator in the neutron transport problem to speedup the simulations. A parallel monolithic multilevel Schwarz preconditioner together with a subspace-based coarsening algorithm is described in Section 3 for both the accelerated transport system and the diffusion system. In Section 4, some numerical tests are carefully studied to demonstrate the performance of the monolithic multilevel Schwarz preconditioner equipped with the subspace-based coarsening algorithm. A few remarks and conclusions are drawn in Section 5.

## **2. Nonlinear diffusion acceleration**

In this section, we present the multigroup neutron transport equations for the criticality calculations, and then study a nonlinear diffusion acceleration

method where a system of diffusion equations is solved to speedup the transport simulations.

### 2.1. Multigroup neutron transport equations

The multigroup neutron transport equations are used to describe the neutron interactions with the background materials in a nuclear reactor system, and they read as follows:

$$\begin{aligned} \vec{\Omega} \cdot \vec{\nabla} \Psi_g(\vec{x}, \vec{\Omega}) + \Sigma_{t,g} \Psi_g(\vec{x}, \vec{\Omega}) &= \sum_{g'=1}^G \int_{\mathcal{S}} \Sigma_{s,g' \rightarrow g} f_{g' \rightarrow g}(\vec{\Omega}' \cdot \vec{\Omega}) \Psi_{g'}(\vec{x}, \vec{\Omega}') d\Omega' \\ &+ \frac{1}{4\pi} \frac{\chi_g}{k} \sum_{g'=1}^G \nu \Sigma_{f,g'} \Phi_{g'}(\vec{x}), \text{ in } \mathcal{D} \times \mathcal{S}, \end{aligned} \quad (1)$$

where  $\Psi_g$  [ $\text{cm}^{-2} \text{s}^{-1} \text{st}^{-1}$ ] are the neutron angular fluxes defined on  $\mathcal{D} \times \mathcal{S}$ ,  $g = 1, 2, \dots, G$ . Here  $G$  is the number of energy groups,  $\mathcal{S}$  is a unit sphere of neutron flying directions and  $\mathcal{D}$  is a 3D spatial domain, for example as shown in Fig. 1. In (1),  $\vec{x} \in \mathcal{D}$  [cm] denotes the independent spatial variable, and  $\vec{\Omega} \in \mathcal{S}$  represents the independent angular variable.  $\Sigma_{t,g}$  [ $\text{cm}^{-1}$ ] is the macroscopic total cross section of the  $g$ th energy group, and  $\Sigma_{s,g' \rightarrow g}$  [ $\text{cm}^{-1}$ ] represents the macroscopic scattering cross section from the  $g'$ th group to the  $g$ th group.  $f_{g' \rightarrow g}$  [ $\text{st}^{-1}$ ] is the scattering phase function that redistributes neutrons from the incoming directions  $\vec{\Omega}'$  to some outgoing directions  $\vec{\Omega}$ . In the second term of the right hand side of (1),  $\chi_g$  denotes the spectrum for both prompt and delayed,  $\nu$  is the averaged number of neutrons emitted per fission,  $\Sigma_{f,g}$  [ $\text{cm}^{-1}$ ] represents the macroscopic fission cross section, and  $\Phi_g$  [ $\text{cm}^{-2} \text{s}^{-1}$ ] are the scalar fluxes that can be calculated by taking an integral of the angular fluxes over the unit sphere

$$\Phi_g \equiv \int_{\mathcal{S}} \Psi_g d\Omega.$$

$k$  is the inverse of eigenvalue (the largest  $k$  is referred to as the neutron multiplication factor). The neutron transport criticality calculations focus on the largest value of  $k$  and the corresponding eigenvalue vector, referred to as the fundamental mode. The first term of (1) is the *streaming term*, the second

is the *collision* term, the third is the *scattering term* and the fourth is the *fission* term. The scattering term couples energy groups through the scattering matrix, and connects angular directions through the integral. Similarly, the fission term couples the angular directions together. The angular and energy coupling makes the neutron transport criticality calculations challenging.

To rewrite (1) as a vector form, we introduce some notations as follows:

$$\Psi \equiv [\Psi_1, \Psi_2, \dots, \Psi_G]^T, \quad (2a)$$

$$\mathbf{L}\Psi \equiv [\mathbb{L}_1\Psi_1, \mathbb{L}_2\Psi_2, \dots, \mathbb{L}_G\Psi_G]^T, \quad \mathbb{L}_g\Psi_g \equiv \vec{\nabla} \cdot \vec{\Omega}\Psi_g + \Sigma_{t,g}\Psi_g, \quad (2b)$$

$$\mathbf{S}\Psi \equiv [\mathbb{S}_1\Psi_1, \mathbb{S}_2\Psi_2, \dots, \mathbb{S}_G\Psi_G]^T, \quad \mathbb{S}_g\Psi_g \equiv \sum_{g'=1}^G \int_S \Sigma_{s,g' \rightarrow g} f_{g' \rightarrow g} \Psi_{g'} d\Omega', \quad (2c)$$

$$\mathbf{F}\Psi \equiv [\mathbb{F}_1\Psi_1, \mathbb{F}_2\Psi_2, \dots, \mathbb{F}_G\Psi_G]^T, \quad \mathbb{F}_g\Psi_g \equiv \frac{1}{4\pi} \chi_g \sum_{g'=1}^G \nu \Sigma_{f,g'} \Phi_{g'}. \quad (2d)$$

Here  $\Psi$  is the angular flux vector consisting of all energy groups.  $\mathbf{L}$ ,  $\mathbf{S}$  and  $\mathbf{F}$  are the streaming-collision operator, the scattering operator and the fission operator, respectively. With the operator notations, we rewrite (1) as

$$\mathbf{L}\Psi = \mathbf{S}\Psi + \frac{1}{k}\mathbf{F}\Psi. \quad (3)$$

Following a standard finite element technique, the weak form of (3) reads as

$$(\mathbf{L}^*\Psi^*, \Psi) + \langle \Psi^*, \bar{\Psi} \rangle^+ - \langle \Psi^*, \bar{\Psi} \rangle^- = (\Psi^*, \mathbf{S}\Psi) + \frac{1}{k} (\Psi^*, \mathbf{F}\Psi), \quad (4)$$

where  $\Psi^*$  is the test function, and  $\mathbf{L}^*$  is the adjoint operator of  $\mathbf{L}$  defined as

$$\mathbf{L}^*\Psi \equiv [\mathbb{L}_1^*\Psi_1, \mathbb{L}_2^*\Psi_2, \dots, \mathbb{L}_G^*\Psi_G]^T, \quad \mathbb{L}_g^*\Psi_g \equiv -\vec{\nabla} \cdot \vec{\Omega}\Psi_g + \Sigma_{t,g}\Psi_g.$$

$(\cdot, \cdot)$  denotes a function inner product over  $\mathcal{D} \times \mathcal{S}$ , for example,

$$(\Psi^*, \Psi) \equiv \sum_{g=1}^G \int_S d\Omega \int_{\mathcal{D}} dx \Psi_g^*(\vec{x}, \vec{\Omega}) \Psi_g(\vec{x}, \vec{\Omega}).$$

$\langle \cdot, \cdot \rangle$  represents the inner product over the boundaries, that is,

$$\langle \mathbf{\Psi}^*, \bar{\mathbf{\Psi}} \rangle^\pm \equiv \sum_{g=1}^G \oint_{\partial\mathcal{D}} dx \int_{\mathcal{S}_{\vec{n}_b}^\pm} d\Omega \left| \vec{\Omega} \cdot \vec{n}_b \right| \Psi_g^*(\vec{x}, \vec{\Omega}) \bar{\Psi}_g(\vec{x}, \vec{\Omega}).$$

Here  $\partial\mathcal{D}$  is the boundary of  $\mathcal{D}$ ,  $\vec{n}_b$  is the outward unit normal vector on  $\partial\mathcal{D}$ , and  $\mathcal{S}_{\vec{n}_b}^\pm = \{\vec{\Omega} \in \mathcal{S} : \vec{\Omega} \cdot \vec{n}_b \gtrless 0\}$ . The vacuum and reflecting boundary conditions are employed in this paper. For the vacuum boundary condition,  $\bar{\mathbf{\Psi}}$  is expressed as

$$\bar{\mathbf{\Psi}} = \begin{cases} \mathbf{\Psi}, & \text{on } \partial\mathcal{D}, \vec{\Omega} \cdot \vec{n}_b \geq 0, \\ \mathbf{0}, & \text{on } \partial\mathcal{D}, \vec{\Omega} \cdot \vec{n}_b < 0. \end{cases}$$

For the reflecting boundary condition,  $\bar{\mathbf{\Psi}}$  is defined as

$$\bar{\mathbf{\Psi}} = \begin{cases} \mathbf{\Psi}, & \text{on } \partial\mathcal{D}, \vec{\Omega} \cdot \vec{n}_b \geq 0, \\ \mathbf{\Psi}_r, & \text{on } \partial\mathcal{D}, \vec{\Omega} \cdot \vec{n}_b < 0, \end{cases}$$

where  $\mathbf{\Psi}_r$  is the reflecting angular fluxes of  $\mathbf{\Psi}$  on  $\vec{\Omega}_r = \vec{\Omega} - 2(\vec{\Omega} \cdot \vec{n}_b)\vec{n}_b$ . The weak form (4) is unstable, and certain stabilizing techniques are required. A stabilizing technique called SAAF (self-adjoint angular flux) [35, 36] is chosen in this work, and the SAAF is very similar to the well-known method SUPG (Streamline upwind/Petrov-Galerkin) [37]. We ignore the description of SAAF here since it has been presented in other literatures [11, 12, 25, 35, 36].

Without introducing any confusion, the same weak form notation is also reused to represent its stabilized version. To simplify the description, the weak form is rewritten as

$$\mathbb{I}(\mathbf{\Psi}^*, \mathbf{\Psi}) - \mathfrak{s}_h(\mathbf{\Psi}^*, \mathbf{\Psi}) = \mathfrak{s}_0(\mathbf{\Psi}^*, \mathbf{\Phi}) + \frac{1}{k} \mathfrak{f}(\mathbf{\Psi}^*, \mathbf{\Phi}), \quad (5)$$

with

$$\mathbb{I}(\mathbf{\Psi}^*, \mathbf{\Psi}) \equiv (\mathbf{L}^* \mathbf{\Psi}^*, \mathbf{\Psi}) + \langle \mathbf{\Psi}^*, \bar{\mathbf{\Psi}} \rangle^+ - \langle \mathbf{\Psi}^*, \bar{\mathbf{\Psi}} \rangle^-,$$

$$\mathfrak{f}(\mathbf{\Psi}^*, \mathbf{\Phi}) \equiv (\mathbf{\Psi}^*, \mathbf{F}\mathbf{\Psi}),$$

and

$$\mathfrak{s}_h(\mathbf{\Psi}^*, \mathbf{\Psi}) + \mathfrak{s}_0(\mathbf{\Psi}^*, \mathbf{\Phi}) \equiv (\mathbf{\Psi}^*, \mathbf{S}\mathbf{\Psi}).$$



Here  $\mathfrak{s}_h$  corresponds to the high order moment fluxes, and  $\mathfrak{s}_0$  corresponds to the zero order moment fluxes that are completely determined by the scalar fluxes.

## 2.2. Diffusion-based acceleration technique

(5) involves the scalar fluxes in the fission term and the scattering term. An alternative way to compute the scalar fluxes is to solve the multigroup neutron diffusion equations. The resulting scalar fluxes and eigenvalue are used to evaluate the fission term and the scattering term of the neutron transport equations. In such a way, the multigroup neutron transport equations are simplified to a linear problem from an eigenvalue problem. It is much cheaper to solve the linear system of equations instead of the eigenvalue problem.

The scalar fluxes are governed by the multigroup neutron diffusion equations,

$$-\vec{\nabla} \cdot D_g \vec{\nabla} \Phi_g(\vec{x}) + \Sigma_{r,g} \Phi_g(\vec{x}) = \sum_{g' \neq g} \Sigma_{s,g' \rightarrow g} \Phi_{g'}(\vec{x}) + \frac{\lambda_g}{k} \sum_{g'=1}^G \nu \Sigma_{f,g'} \Phi_{g'}(\vec{x}), \text{ in } \mathcal{D}, \quad (6)$$

where  $D_g$  [cm] is the diffusion coefficient, and  $\Sigma_{r,g} \equiv \Sigma_{t,g} - \Sigma_{s,g \rightarrow g}$ , in [ $\text{cm}^{-1}$ ], is the macroscopic removal cross section. The first term is the *diffusion term* and the second is the *removal term*. The first term on the right hand side is the *scattering term*, which couples the scalar fluxes together through the scattering matrix. The last term is the *fission term*. For conciseness, we also write Eq. (6) in a vector form,

$$-\vec{\nabla} \cdot \vec{\mathbf{J}} + \mathbf{L}_r \Phi = \mathbf{S}_d \Phi + \frac{1}{k} \mathbf{F}_0 \Phi, \quad (7)$$

where

$$\begin{aligned} \vec{\mathbf{J}} &\equiv [\vec{J}_1, \vec{J}_2, \dots, \vec{J}_G]^T, \quad \vec{J}_g \equiv D_g \vec{\nabla} \Phi_g, \\ \mathbf{L}_r \Phi &\equiv [\mathbb{L}_{r,1} \Phi_1, \mathbb{L}_{r,2} \Phi_2, \dots, \mathbb{L}_{r,G} \Phi_G]^T, \quad \mathbb{L}_{r,g} \Phi_g \equiv \Sigma_{r,g} \Phi_g, \\ \mathbf{S}_d \Phi &\equiv [\mathbb{S}_{d,1} \Phi_1, \mathbb{S}_{d,2} \Phi_2, \dots, \mathbb{S}_{d,G} \Phi_G]^T, \quad \mathbb{S}_{d,g} \equiv \sum_{g' \neq g} \Sigma_{s,g' \rightarrow g} \Phi_{g'}, \end{aligned}$$

and

$$\mathbf{F}_0 \Phi \equiv \left[ \mathbb{F}_{0,1} \Phi_1, \mathbb{F}_{0,2} \Phi_2, \dots, \mathbb{F}_{0,G} \Phi_G \right]^T, \quad \mathbb{F}_{0,g} \Phi_g \equiv \chi_g \sum_{g'=1}^G \nu_{\Sigma_{f,g'}} \Phi_{g'}.$$

Multiply (7) by a test function  $\Phi^*$  and integrate by parts, then we have the weak form of (7) as follows

$$\mathbb{b}_{\text{diff}}(\Phi^*, \Phi) = \frac{1}{k} \mathbb{f}_{\text{diff}}(\Phi^*, \Phi), \quad (8)$$

with

$$\mathbb{b}_{\text{diff}}(\Phi^*, \Phi) = \left( \vec{\nabla} \Phi^*, \mathbb{D} \vec{\nabla} \Phi \right)_{\mathcal{D}} + \left\langle \Phi^*, \frac{1}{4} \Phi \right\rangle_{\partial \mathcal{D}} + (\Phi^*, \mathbf{L}_r \Phi)_{\mathcal{D}} - (\Phi^*, \mathbf{S}_d \Phi)_{\mathcal{D}},$$

and

$$\mathbb{f}_{\text{diff}}(\Phi^*, \Phi) = (\Phi^*, \mathbf{F}_0 \Phi)_{\mathcal{D}},$$

where  $(\cdot, \cdot)_{\mathcal{D}}$  denotes a function inner product over  $\mathcal{D}$ , and  $\langle \cdot, \cdot \rangle_{\partial \mathcal{D}}$  represents the function inner product on  $\partial \mathcal{D}$ . In (8), the Robin boundary condition is used,

$$\frac{\Phi_g}{4} + \mathbb{D}_g \vec{\nabla} \Phi_g \cdot \vec{n}_b = 0, \quad \text{on } \partial \mathcal{D}.$$

For accelerating the solution of (5), the low-order diffusion equations (8) need additional nonlinear closure terms so that the low-order scalar fluxes become identical to the projection of the high order solution into the low order space when the algorithm converges. The following closure terms are employed when (5) is stabilized with the SAAF method and discretized in angle using the discrete ordinates (SN),

$$\mathbb{C}[\Psi](\Phi^*, \Phi) \equiv \left( \vec{\nabla} \Phi^*, \tilde{\mathbf{D}} \Phi \right)_{\mathcal{D}} + \langle \Phi^*, \gamma \Phi \rangle_{\partial \mathcal{D}}. \quad (9)$$

Here

$$\tilde{\mathbf{D}} \equiv [\tilde{D}_1, \tilde{D}_2, \dots, \tilde{D}_G]^T,$$

with

$$\tilde{D}_g = \frac{\int_{\mathcal{S}} \left( \tau_g \vec{\Omega} \vec{\Omega} \cdot \vec{\nabla} \Psi_g + (\tau_g \Sigma_{t,g} - 1) \vec{\Omega} \Psi_g - \tau_g \sum_{g'=1}^G \Sigma_{s,1}^{g' \rightarrow g} \vec{\Omega} \Psi_{g'} - \mathbb{D}_g \vec{\nabla} \Psi_g \right) d\Omega}{\int_{\mathcal{S}} \Psi_g d\Omega},$$

and

$$\gamma \equiv [\gamma_1, \gamma_2, \dots, \gamma_G]^T,$$

with

$$\gamma_g = \frac{\int_{\vec{\Omega} \cdot \vec{n}_b > 0} |\vec{\Omega} \cdot \vec{n}_b| \Psi_g d\Omega}{\int_S \Psi_g d\Omega} - \frac{1}{4}.$$

Here  $\Sigma_{s,1}^{g' \rightarrow g}$  is the first order of scattering cross section (see more details in [25]), and  $\tau_g$  is the stabilization parameter defined as

$$\tau_g = \begin{cases} \frac{1}{c\Sigma_{t,g}}, & ch\Sigma_{t,g} \geq \varsigma, \\ \frac{h}{\varsigma}, & ch\Sigma_{t,g} < \varsigma, \end{cases} \quad (10)$$

where  $h$  is the characteristic length of a mesh element,  $\varsigma$  is usually chosen to be a constant of 0.5 and  $c$  is a constant as well (1.0 by default). A detailed explanation of (10) can be found in [25]. With these notations, the nonlinear diffusion acceleration scheme is summarized in Alg. 2.1.

The low order diffusion equations (12) are discretized using the first order continuous finite element [24, 25], and the multigroup transport equations (11) are discretized with the first order finite element method in space and with the SN scheme in angle [11, 12, 25]. After the spatial and angular discretizations, the multigroup transport equations at line 4 of Alg. 2.1 correspond to a linear system of equations since the fission term and part of the scattering term are evaluated using the scalar fluxes and the eigenvalue computed in the low order diffusion system. An algebraic generalized eigenvalue system is generated after the spatial discretization of the low order diffusion system. The low order diffusion system is challenging to solve since the extra closure terms can have a significant impact on diffusion coefficients, and meanwhile the high order transport system is expensive to solve due to the high dimensionality. We next study a novel monolithic multilevel Schwarz method that is capable of solving both the low order diffusion system and the high order transport system while constructing coarse spaces in an efficient way.

---

**Algorithm 2.1** Nonlinear diffusion acceleration method

---

1: Solve the low-order diffusion system without the closure terms:

$$\mathbb{b}_{\text{diff}}(\Phi^*, \Phi^{(0)}) = \frac{1}{k^{(0)}} \mathbb{f}_{\text{diff}}(\Phi^*, \Phi^{(0)})$$

2:  $n = 0$

3: **for**  $n < \max_{\text{nda}}$  and  $\epsilon_1 > \text{tol}$  **do**

4: Solve the transport system:

$$\mathbb{I}(\Psi^*, \Psi^{(n+1)}) - \mathbb{s}_h(\Psi^*, \Psi^{(n)}) = \mathbb{s}_0(\Psi^*, \Phi^{(n)}) + \frac{1}{k^{(n)}} \mathbb{f}(\Psi^*, \Phi^{(n)}) \quad (11)$$

5: Update the coefficients,  $\tilde{\mathbf{D}}$ , of the closure terms

6: Solve the diffusion system with the closure terms:

$$\mathbb{b}_{\text{diff}}(\Phi^*, \Phi^{(n+1)}) + \mathbb{C}[\Psi^{(n+1)}](\Phi^*, \Phi^{(n+1)}) = \frac{1}{k^{(n+1)}} \mathbb{f}_{\text{diff}}(\Phi^*, \Phi^{(n+1)}) \quad (12)$$

7: Calculate  $\epsilon_1 = \left| \Phi^{(n+1)} - \Phi^{(n)} \right|$

8:  $n+ = 1$

9: **end for**

---

### 3. Monolithic multilevel Schwarz preconditioner

In this section, we briefly describe a parallel monolithic algorithm framework, and then study a multilevel Schwarz preconditioner equipped with a subspace-based coarsening approach for both the transport equations and the diffusion equations.

#### 3.1. Parallel Newton accelerated eigenvalue solver

After the spatial discretization of (12), an algebraic generalized eigenvalue system reads as

$$\mathcal{A}\Phi = \frac{1}{k}\mathcal{B}\Phi, \quad (13)$$

where  $\mathcal{A}$  is the matrix consisting of the first and the second terms of (12), and  $\mathcal{B}$  represents the matrix corresponding to the fission term.  $\mathcal{A}$  and  $\mathcal{B}$  are not formed explicitly for saving memory. The notation  $\Phi$  is reused to denote the discretized version of the scalar fluxes, that is, it is a vector whose components are the finite element nodal values. The neutron transport criticality calculations target at the largest value of  $k$  in (13).

One of the simplest approaches to calculate the largest value of  $k$  is inverse power iteration [1, 6], which starts with an initial guess and computes a new approximation with solving a linear system of equations. More precisely, with a given initial pair  $(\Phi_0, k_0 = \|\mathcal{B}\Phi_0\|)$ , a new approximation  $(\Phi_{n+1}, k_{n+1})$ ,  $n = 0, 1, \dots, \max_{\text{eigen}}$ , is obtained using the following steps:

$$\mathcal{A}\Phi_{n+1} = \mathcal{B}\Phi_n, \quad (14a)$$

$$k_{n+1} = \|\mathcal{B}\Phi_{n+1}\|, \quad (14b)$$

$$\mathcal{B}\Phi_{n+1} \leftarrow \frac{1}{k_{n+1}}\mathcal{B}\Phi_{n+1}. \quad (14c)$$

Here the first step solves a linear system of equations, the second step calculates the norm of the right hand side as a new eigenvalue approximation, and finally the right hand side is scaled in place.

The inverse power iteration converges slowly when the smallest and the second smallest eigenvalues are close to each other, which often occurs in realistic problems. To overcome this difficulty, an inexact Newton method [19] is employed to accelerate the inverse power iteration by reforming (14) as a nonlinear system of equations,

$$\mathcal{F}(\Phi) \equiv \mathcal{A}\Phi - \frac{1}{\|\mathcal{B}\Phi\|}\mathcal{B}\Phi = 0. \quad (15)$$

Newton starts with an initial guess  $\Phi_0$  that, in this paper, is calculated with a few inverse power iterations, and then a new approximation solution,  $\Phi_{n+1}$ ,  $n = 0, 1, \dots, \max_{\text{newton}}$ , is updated as follows,

$$\Phi_{n+1} = \Phi_n + \alpha_n \Delta \Phi_n. \quad (16)$$

Here  $\alpha_n$  is a Newton step length calculated using a backtracking line search scheme [38], and  $\Delta \Phi_n$  is obtained by solving the Jacobian system

$$\mathcal{J}(\Phi_n) \Delta \Phi_n = -\mathcal{F}(\Phi_n), \quad (17)$$

where  $\mathcal{J}(\Phi_n)$  is the Jacobian matrix evaluated at  $\Phi_n$  and  $\mathcal{F}(\Phi_n)$  is the nonlinear function residual at  $\Phi_n$ . Explicitly forming  $\mathcal{J}$  is memory intensive since there exists significant coupling among variables through the scattering term and the fission term. In addition, the derivatives of  $1/\|\mathcal{B}\Phi\|$  is difficult to compute. To fix these issues,  $\mathcal{J}$  is carried out in a matrix-free manner, that is, the action of  $\mathcal{J}$  on a vector  $\Delta \Phi_n$  is implemented via finite difference

$$\mathcal{J}(\Phi_n) \Delta \Phi_n = \frac{\mathcal{F}(\Phi_n + \beta \Delta \Phi_n) - \mathcal{F}(\Phi_n)}{\beta},$$

where  $\beta$  is a small parameter calculated using a strategy proposed in [39]. The resulting inexact Newton is often referred to as ‘‘Jacobian-free Newton method’’ [20, 21] that is also very useful when the Jacobian is difficult to form due to for example the complicated physics procedures under a multiphysics environment. We summarize the Newton accelerated eigenvalue solver in Alg. 3.1, and will discuss the preconditioning technique in next section. Note that the

---

**Algorithm 3.1** Newton accelerated eigenvalue solver

---

- 1: Initialize:  $\tilde{\Phi}_0, \tilde{k}_0 = \|\mathcal{B}\tilde{\Phi}_0\|$
  - 2: **for**  $n = 0, 1, 2, \dots, \max_{\text{eigen}}$  **do**
  - 3:   Solve a linear sytem:  $\mathcal{A}\tilde{\Phi}_{n+1} = \mathcal{B}\tilde{\Phi}_n$
  - 4:   Update eigenvalue:  $\tilde{k}_{n+1} = \|\mathcal{B}\tilde{\Phi}_{n+1}\|$
  - 5:   Scale right hand side:  $\mathcal{B}\tilde{\Phi}_{n+1} \leftarrow \frac{1}{\tilde{k}_{n+1}}\mathcal{B}\tilde{\Phi}_{n+1}$
  - 6: **end for**
  - 7: Set an initial guess for Newton:  $\Phi_0 = \tilde{\Phi}_n$
  - 8: n=0
  - 9: **for**  $n < \max_{\text{newton}}$  and  $\epsilon > \text{tol}_{\text{newton}}$  **do**
  - 10:   Solve the Jacobian sytem:  $\mathcal{J}(\Phi_n)\Delta\Phi_n = -\mathcal{F}(\Phi_n)$
  - 11:   Perform a line search to compute  $\alpha_n$
  - 12:   Update solution:  $\Phi_{n+1} = \Phi_n + \alpha_n\Delta\Phi_n$
  - 13:    $\epsilon = \|\mathcal{F}(\Phi_{n+1})\| / \|\mathcal{F}(\Phi_0)\|$
  - 14:   n += 1
  - 15: **end for**
-

Newton-Krylov method has been widely and successfully employed for non-linear systems of equations arising from different engineering areas; e.g., elasticity problems [32], incompressible flows [40], fluid-structure interactions [33, 41, 42, 43]. In this work, the Newton-Krylov method is employed to solve the eigenvalue problems.

### 3.2. Single-component grid based coarse spaces

In this section, we present a monolithic multilevel method for (11), (14a) and (17), where a subspace-based coarsening algorithm is studied to generate a sequence of Single-component Grid based coarse spaces (SG coarse spaces) for improving the parallel performance.

Three linear systems of equations, (11), (14a) and (17), need to be solved, and we hence denote them in an unified general linear system of equations,

$$\mathbf{A}\mathbf{x} = \mathbf{b}, \quad (18)$$

where  $\mathbf{A} = \mathcal{A}$  in (14a),  $\mathbf{A} = \mathcal{J}$  in (17), and  $\mathbf{A}$  corresponds to the discretized version of  $\mathbf{l}$  in (11).  $\mathbf{x}$  is the nodal values of  $\Phi$  in (14a) and (17), and corresponds to the discretized version of  $\Psi$  in (11). The linear system (18) is solved using an iterative Krylov subspace method; e.g., GMRES [44], and an efficient preconditioner is required to speedup the convergence. In the current study, a standard restarted GMRES from PETSc [16] is chosen, and no change was made to GMRES. The restart number of GMRES is 30 by default in PETSc. While other Krylov subspace methods [45] are possible for solving the Jacobian system, we consider only GMRES in the current study. GMRES was chosen as the default linear solver in the multiphysics framework MOOSE [46] because it appears sufficiently general for a wide range of multiphysics problems.

The right preconditioned linear system is rewritten as

$$\mathbf{A}\mathbf{M}^{-1}\mathbf{M}\mathbf{x} = \mathbf{b}, \quad (19)$$

where  $\mathbf{M}$  is a preconditioning matrix, and  $\mathbf{M}^{-1}$  is a preconditioning process.  $\mathbf{M}$  is an approximation to  $\mathcal{A}$  in (14a), to  $\mathcal{J}$  in (17), and  $\mathbf{M}$  corresponds to the



discretized version of  $\mathbb{L}$  in (11). The preconditioned system (19) is computed in two steps,

$$\mathbf{A}\mathbf{M}^{-1}\tilde{\mathbf{x}} = \mathbf{b}, \quad (20a)$$

$$\mathbf{M}\mathbf{x} = \tilde{\mathbf{x}}, \quad (20b)$$

where  $\tilde{\mathbf{x}}$  is an intermediate auxiliary vector. In (20), the preconditioner is applied from the right side, but we want to mention that the preconditioner can be applied from the left side as well. In general, a preconditioning process aims at a correction with solving the residual equations,

$$\mathbf{M}\mathbf{e} = \mathbf{r}, \quad (21)$$

where  $\mathbf{e}$  is a correction vector, and  $\mathbf{r}$  is the residual vector from the outer solver, GMRES.

In this paper, we employ a multilevel Schwarz preconditioner for the solution of (21). To describe the multilevel preconditioner, we partition the fine mesh  $\mathcal{D}_h$ , a triangulation of  $\mathcal{D}$ , into  $np$  submeshes,  $\mathcal{D}_{h,i}$ ,  $i = 1, 2, \dots, np$ . Here  $np$  is the number of processor cores. The mesh is partitioned using a hierarchical partitioning approach [32, 47]. The hierarchical partitioning takes into consideration that there are multiple processor cores per each compute node on modern supercomputers and these cores share the same chunk of memory. The hierarchical partitioning generally consists of two steps (even though it has been extended to a multilevel version [47]). The mesh is first partitioned into  $np_1$  submeshes ( $np_1$  is often the number of compute nodes), and then each submesh is further divided into  $np_2$  small submeshes ( $np_2$  is often the number of processor cores per compute node). The hierarchical partitioning is able to minimize the communication between compute nodes since only compute-node boundary cores need to send messages across the network, and the messages within the same compute node are efficiently handled by a modern MPI implementation. A detailed discussion on the hierarchical partitioning can be found in [32, 47]. A hierarchical partitioning example is shown in Fig. 1, where a 3D mesh is parti-



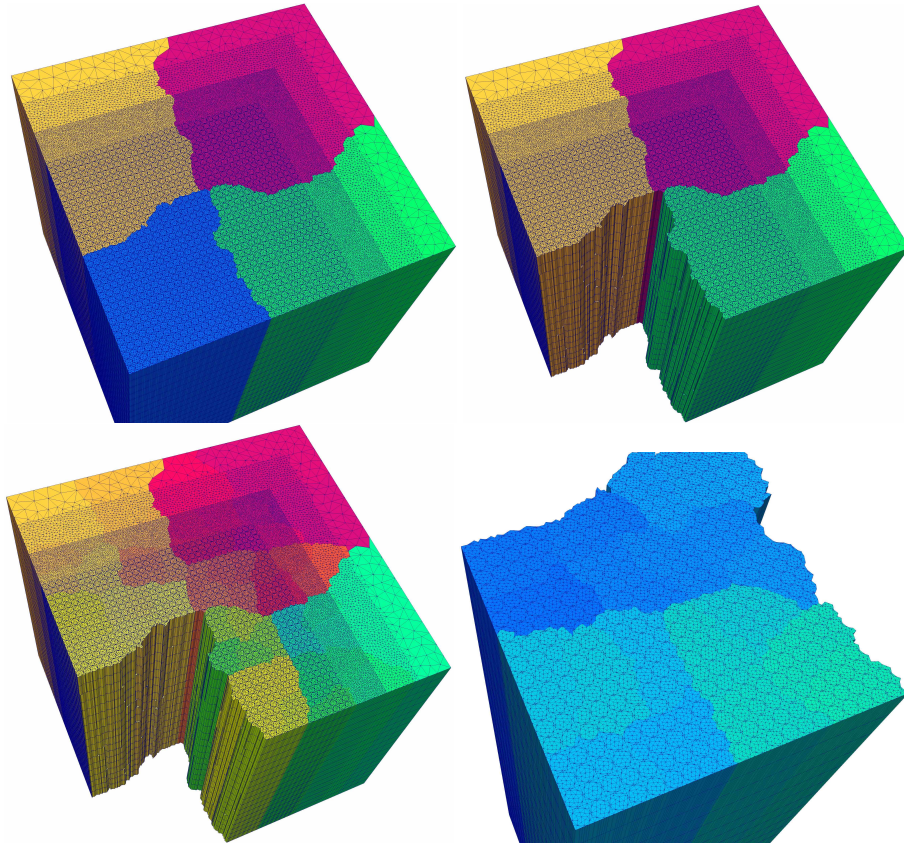


Figure 1: Demonstration of partitioning a mesh into 80 submeshes using the hierarchical partitioning approach. Assume there are 4 compute nodes available, and each compute node has 20 processor cores. The mesh is partitioned into 4 submeshes, and each submesh is further partitioned into 20 small submeshes. We have 80 submeshes in total at the end. First row: a mesh is partitioned into 4 submeshes; second row: each submesh is divided into 20 small submeshes. For the visualization purpose, the first submesh is taken off in the right picture of the first row. The right picture of the second row is the partition of the first submesh into 20 small submeshes.



Figure 2: 1D mesh used for the demonstration of constructing overlapping submatrices.

2. The submatrices with  $\delta = 0$  are written as

$$(\mathbf{M}_{1D})_1^0 = \begin{bmatrix} m_{11} & m_{12} & & & \\ m_{21} & m_{22} & m_{23} & & \\ & m_{32} & m_{33} & m_{34} & \\ & & m_{43} & m_{44} & \end{bmatrix}, \quad (23)$$

and

$$(\mathbf{M}_{1D})_2^0 = \begin{bmatrix} m_{55} & m_{56} & \\ m_{65} & m_{66} & m_{67} \\ & m_{76} & m_{77} \end{bmatrix}. \quad (24)$$

When  $\delta = 1$  and 2, the corresponding overlapping submatrices are written as, respectively,

$$(\mathbf{M}_{1D})_1^1 = \begin{bmatrix} m_{11} & m_{12} & & & \\ m_{21} & m_{22} & m_{23} & & \\ & m_{32} & m_{33} & m_{34} & \\ & & m_{43} & m_{44} & m_{45} \\ & & & m_{54} & m_{55} \end{bmatrix}, \quad (25)$$

$$(\mathbf{M}_{1D})_2^1 = \begin{bmatrix} m_{44} & m_{45} & & & \\ m_{54} & m_{55} & m_{56} & & \\ & m_{65} & m_{66} & m_{67} & \\ & & m_{76} & m_{77} & \end{bmatrix}, \quad (26)$$

$$(\mathbf{M}_{1D})_1^2 = \begin{bmatrix} m_{11} & m_{12} & & & & \\ m_{21} & m_{22} & m_{23} & & & \\ & m_{32} & m_{33} & m_{34} & & \\ & & m_{43} & m_{44} & m_{45} & \\ & & & m_{54} & m_{55} & m_{56} \\ & & & & m_{65} & m_{66} \end{bmatrix}, \quad (27)$$

and

$$(\mathbf{M}_{1D})_2^2 = \begin{bmatrix} m_{33} & m_{34} & & & & & & & \\ m_{43} & m_{44} & m_{45} & & & & & & \\ & m_{54} & m_{55} & m_{56} & & & & & \\ & & m_{65} & m_{66} & m_{67} & & & & \\ & & & m_{76} & m_{77} & & & & \end{bmatrix}. \quad (28)$$

Note, the 1D mesh is used for the visualization only, and the submatrices are constructed algebraically without using a mesh.

With these notations, a one-level restricted Schwarz preconditioner [40, 50] is defined as follows,

$$\mathbf{M}_{\text{one}}^{-1} = \sum_{i=1}^{np} (\mathbf{R}_i^0)^T (\mathbf{M}_i^\delta)^{-1} \mathbf{R}_i^\delta, \quad \mathbf{M}_i^\delta = \mathbf{R}_i^\delta \mathbf{M} (\mathbf{R}_i^\delta)^T, \quad (29)$$

where  $(\mathbf{M}_i^\delta)^{-1}$  represents the submesh solver that is SOR (successive over-relaxation) in this paper.  $\mathbf{R}_i^\delta$  is not necessarily implemented as a matrix; e.g., in PETSc [16] it is implemented as a map from the global vector to the local overlapping subvector. We refer  $\mathbf{M}_{\text{one}}^{-1}$  to as a monolithic preconditioner since it handles all unknowns simultaneously, which is fundamentally different from a traditional Gauss-Seidel approach. Different variants of domain composition methods can be found in other literatures [48, 49].

$\mathbf{M}_{\text{one}}^{-1}$  works for many problems, but coarse spaces are often required to enhance the preconditioner when the number of processor cores is large or when the system is ill-conditioned. In general, there are two approaches to generate coarse spaces. The first approach is to coarsen the fine mesh to generate coarse finite element meshes based on which the coarse spaces are constructed. This geometric method has been successfully applied to many applications; e.g., elasticity problems [32], fluid-structure interactions [33, 41, 42, 43]. The other approach is to avoid coarsening the fine mesh, instead, coarse spaces are generated using the matrix only. The first approach is referred to as “geometric multilevel method”, and the second approach is referred to as “algebraic multilevel method”. We consider the algebraic approach here since it has an out-of-box

nature. Note that no coarse finite element meshes are constructed in the algebraic multilevel method, and the required coarse spaces are built algebraically with a matrix coarsening algorithm to be discussed shortly. However, algebraically constructing coarse spaces is expensive and sometimes unscalable. In order to make the overall algorithm scalable, we explore the matrix structures to reduce the cost of coarse space construction.

For saving memory, the preconditioning matrix ignores the energy coupling in the diffusion system, and drops the energy and angular coupling in the transport system. If the matrix was ordered component-by-component, we would have a block diagonal matrix,

$$\mathbf{M} = \begin{bmatrix} M_1 & & & \\ & M_2 & & \\ & & \ddots & \\ & & & M_{n_{\text{comp}}} \end{bmatrix}, \quad (30)$$

where  $n_{\text{comp}}$  is the number of components. In the low order diffusion system, each component corresponds to an energy group, that is,  $n_{\text{comp}} = G$ . In the transport system, each component corresponds to an angular direction of a given energy group, that is,  $n_{\text{comp}} = G \times N_d$ . In either the diffusion system or the transport system,  $M_j, j = 1, 2, \dots, n_{\text{comp}}$ , is a spatial matrix.

Component matrices (spatial matrices),  $M_j, j = 1, 2, \dots, n_{\text{comp}}$ , correspond to the discretization of partial differential equations on  $\mathcal{D}_h$ . The structures of spatial matrices are similar to each other since they correspond to the same partial differential equation operators, and the numeric values of spatial matrices are different from each other because of different materials. Based on these observations, we coarsen a single-component matrix, e.g.,  $M_1$ , instead of the full matrix,  $\mathbf{M}$ , to generate a sequence of subinterpolations that are reused for all other components. The subinterpolations generated based on a single-component matrix are referred to as “Single-component Grid based interpolations” (SG interpolations). More precisely, we use GAMG [16] or BoomerAMG [34] to coarsen  $M_1$  to build a  $L$ -level hierarchy consisting of  $(L - 1)$  subinter-

polations,  $P_{l+1}^l$ ,  $l = 1, 2, \dots, L - 1$ . The coarsening process based on a single-component matrix to generate a sequence of SG interpolations is referred to as “subspace-based coarsening”. To define the full interpolations, we introduce a restriction operator that extracts a subvector  $r_j$  for component  $j$  from the full vector  $\mathbf{r}$ ,

$$r_j = R_j \mathbf{r} = [I_j \ 0] \begin{bmatrix} r_j \\ \mathbf{r} \setminus r_j \end{bmatrix}, j = 1, 2, \dots, n_{\text{comp}}.$$

Here  $I_j$  is an identity matrix, and  $\mathbf{r} \setminus r_j$  denotes all the elements in  $\mathbf{r}$  but not in  $r_j$ .  $R_j$  can be defined on all levels, and it is rewritten as  $R_j^l$  for the  $j$ th component on the  $l$ th level. The full interpolations are then written as

$$\mathbf{P}_{l+1}^l = \sum_{j=1}^{n_{\text{comp}}} (R_j^l)^T P_{l+1}^l R_j^{l+1}, l = 1, 2, \dots, L - 1. \quad (31)$$

The coarse operators are defined using the Galerkin method with  $\mathbf{P}_{l+1}^l$ , that is,

$$\mathbf{M}^{l+1} = (\mathbf{P}_{l+1}^l)^T \mathbf{M}^l \mathbf{P}_{l+1}^l. \quad (32)$$

Here  $\mathbf{M}^1 = \mathbf{M}$  is the finest level operator. The coarse spaces defined in (32) are referred to as “Single-component Grid based coarse spaces” (SG coarse spaces) since they are constructed based on the SG interpolations.

Similarly, the one-level method can be defined on each level, and these one-level preconditioners are denoted as  $(\mathbf{M}_{\text{one}}^l)^{-1}$  ( $l = 1, 2, \dots, L$ ). The multilevel method constructed with the subspace-based coarsening algorithm is referred to as “Single-component Grid based Multilevel Additive Schwarz Method” (SGMASM), shown in Alg. 3.3. The method using the unmodified standard coarse spaces is denoted as “Multilevel Additive Schwarz Method” (MASM), shown in Alg 3.4. For saving memory, the interpolations in (31) are implemented without storing duplicated values in a specific matrix format in PETSc [16], and the sparse matrix triple products in (32) are carried out using an all-at-once approach [51]. Note, in Alg. 3.3, the SG coarse spaces are generated based on the first component matrix. In practice, any component matrix can be chosen to generate a sequence of SG coarse spaces, and it is an user-specified parameter in software.

---

**Algorithm 3.2** Application of multilevel preconditioner

---

```
1: procedure PCAPPLY( $\mathbf{M}^l, \mathbf{e}^l, \mathbf{r}^l$ )
2:   if  $l = L$  then
3:     Solve  $\mathbf{M}^L \mathbf{e}^L = \mathbf{r}^L$  with a direct solver redundantly on each compute
       node or each processor core
4:   else
5:     Pre-solve  $\mathbf{M}^l \mathbf{e}^l = \mathbf{r}^l$  for  $\mathbf{e}^l$  using a  $(\mathbf{M}_{\text{one}}^l)^{-1}$  preconditioned iterative
       method
6:     Set  $\tilde{\mathbf{r}}^l = \mathbf{r}^l - \mathbf{M}^l \mathbf{e}^l$ 
7:     Apply restriction:  $\tilde{\mathbf{r}}^{l+1} = (\mathbf{P}_{l+1}^l)^T \tilde{\mathbf{r}}^l$ 
8:     Call PCApply( $\mathbf{M}^{l+1}, \mathbf{z}^{l+1}, \tilde{\mathbf{r}}^{l+1}$ )
9:     Apply interpolation:  $\mathbf{z}^l = \mathbf{P}_{l+1}^l \mathbf{z}^{l+1}$ 
10:    Apply correction:  $\mathbf{e}^l = \mathbf{e}^l + \mathbf{z}^l$ 
11:    Post-solve  $\mathbf{M}^l \mathbf{e}^l = \mathbf{r}^l$  for  $\mathbf{e}^l$  using a  $(\mathbf{M}_{\text{one}}^l)^{-1}$  preconditioned itera-
       tive method
12:   end if
13: end procedure
```

---



---

**Algorithm 3.3** Multilevel Schwarz preconditioner constructed with the subspace-based coarsening algorithm (SGMASM)

---

```

1: procedure PCSETUP(M)
2:   Extract a component matrix  $M_1$  from M in parallel
3:   Coarsen  $M_1$  and generate  $(L - 1)$  subinterpolations  $P_{l+1}^l$ 
4:   for  $l = 1, 2, \dots, L - 1$  do
5:     Construct the  $l$ th full interpolation:  $\mathbf{P}_{l+1}^l = \sum_{j=1}^{n_{\text{comp}}} (R_j^l)^T P_{l+1}^l R_j^{l+1}$ 
6:   end for
7:   for  $l = 1, 2, \dots, L - 1$  do
8:     Build the  $(l + 1)$ th coarse matrix:  $\mathbf{M}^{l+1} = (\mathbf{P}_{l+1}^l)^T \mathbf{M}^l \mathbf{P}_{l+1}^l$ 
9:   end for
10:  Return  $\{\mathbf{M}^{l+1}\}$  and  $\{\mathbf{P}_{l+1}^l\}, l = 1, 2, \dots, L - 1$ 
11: end procedure
12: Call PCApply( $\mathbf{M}^1, \mathbf{e}^1, \mathbf{r}^1$ ) ▷ Alg. 3.2
13: Return  $\mathbf{e}^1$ 

```

---



---

**Algorithm 3.4** Traditional multilevel Schwarz preconditioner (MASM)

---

```

1: procedure PCSETUP(M)
2:   Coarsen M and generate  $(L - 1)$  interpolations  $\mathbf{P}_{l+1}^l$  and  $(L - 1)$  coarse
   matrices  $\mathbf{M}^{l+1}$ 
3:   Return  $\{\mathbf{M}^{l+1}\}$  and  $\{\mathbf{P}_{l+1}^l\}, l = 1, 2, \dots, L - 1$ 
4: end procedure
5: Call PCApply( $\mathbf{M}^1, \mathbf{e}^1, \mathbf{r}^1$ ) ▷ Alg. 3.2
6: Return  $\mathbf{e}^1$ 

```

---

#### 4. Numerical results

In this section, we report the performance of the proposed algorithm in terms of the compute time and the memory usage. The C5G7 MOX 3D benchmark is employed here as a test case, and its configuration is shown in Fig. 3, where different pin colors correspond to different materials; e.g., UO<sub>2</sub>, guide tube, fission chamber, MOX 4.3%, MOX 7.0%, MOX 8.7%, and control rod. The overall dimensions of the domain are  $64.26 \times 64.26 \times 64.26$  cm, where each fuel assembly is  $21.42 \times 21.42 \times 42.84$  cm. A fuel assembly consists of a  $17 \times 17$  lattice of pin cells, where the side length of each pin cell is 1.26 cm and the radius of the fuel pins and guide tubes is 0.54 cm. The reflected boundary conditions are applied to the front, the left and the bottom boundaries, and the vacuum boundary conditions are applied to the back, the right and the top boundaries. The seven-group set of cross sections are often chosen to test the algorithm performance since the corresponding problem is difficult to solve. More details of the benchmark configuration can be found in literatures [52, 53]. The computed eigenvalue is 1.141932, and the eigen flux moments for the second and the sixth groups are shown in Fig. 4.

The preconditioner is implemented in PETSc [16] as part of this work, and the subspace-based coarsening algorithm is implemented based on Boomer-AMG [34]. The angular and spatial discretizations are implemented in Rattlesnake [25] that is on top of MOOSE [54, 46] and libMesh [55]. The numerical experiments are carried out on a supercomputer at INL (Idaho National Laboratory), where each compute node has two 20-core processors with 2.4 GHz and the compute nodes are connected by an OmniPath network.

For simplifying the discussion, we define some notations that will be used in the rest of paper. “Mem” represents the estimated memory usage per processor core in Megabyte (M), “Its<sub>Newton</sub>” is the averaged number of Newton iterations per Picard iteration for the diffusion system, “Its<sub>linear</sub>” is the averaged number of GMRES iterations per Newton step in the diffusion system, “Its<sub>sweep</sub>” denotes the averaged number of GMRES iterations per Picard itera-

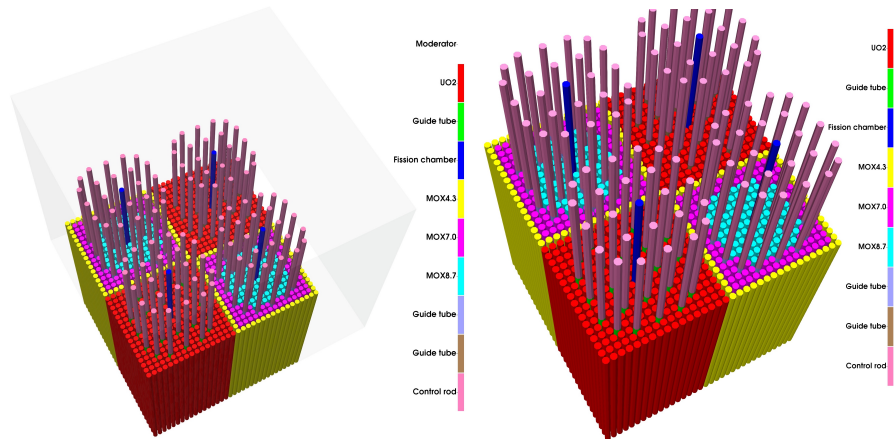


Figure 3: C5G7 3D benchmark configuration. Left: four assemblies at the front bottom of a  $64.26 \times 64.26 \times 64.26$  cm cube; right: four assemblies and control rods. Different pin colors correspond to different materials, e.g., UO<sub>2</sub>, guide tube, fission chamber, MOX 4.3%, MOX 7.0%, MOX 8.7%, and control rod.

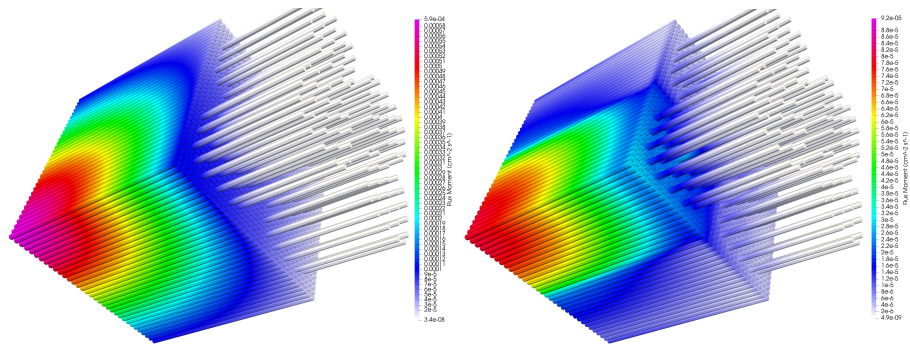


Figure 4: Flux moments. Left: the first group flux moment; right: the sixth group flux moment.

tion in the transport system, “Time<sub>low</sub>” represents the compute time spent on the diffusion solver, “Time<sub>high</sub>” is the compute time on the transport solver, “Time<sub>T</sub>” is the total compute time for the overall simulation, and “EFF” is the parallel efficiency with respect to the number of processor cores. “Time<sub>ksp</sub>” is the total compute time on the linear solver, “Time<sub>pCA</sub>” represents the total compute time on the preconditioner application, “Time<sub>pCS</sub>” is the total compute time on the preconditioner setup, “Time<sub>MF</sub>” denotes the compute time on the matrix-free matrix-vector operations, “Time<sub>Func</sub>” is the time spent on the function evaluations, “Time<sub>Jac</sub>” represents the compute time on the Jacobian evaluations, and “Time<sub>LS</sub>” is the time consumed by the line search routine. All compute times are reported in second (s). A relative tolerance of  $10^{-5}$  is chosen for the linear solver of the transport system. In the diffusion system, Newton is stopped when a relative tolerance of  $10^{-3}$  is met, and the relative tolerance of the linear solver is  $10^{-2}$ . Below we start to discuss the algorithm robustness with respect to different parameters; e.g., subdomain overlapping size, strength matrix threshold and the number of aggressive coarsening levels.

#### 4.1. Subdomain overlapping size

A subdomain overlapping size plays an important role on domain decomposition methods. A larger overlapping size often leads to a better convergence in terms of the number of GMRES iterations, meanwhile the resulting preconditioner also consumes more memory and involves more communication. We need to take the iteration count, the memory usage and the communication into consideration to choose an optimal overlapping size, and the optimal overlapping size is often problem dependent.

In this test, we report the parallel performance of the proposed algorithm with respect to different overlapping sizes. A Gauss Chebyshev angular quadrature scheme with 32 directions is employed. A mesh with 832,371 nodes and 1,567,944 elements is used for both the diffusion system and the transport system. The diffusion system has 5,826,597 unknowns, and the transport system has 186,451,104 unknowns. The numerical results are summarized in Table 1.

Table 1: Parallel performance with respect to different subdomain overlapping sizes. The transport system with 186,451,104 unknowns is accelerated by the low order diffusion system with 5,826,597 unknowns.

$np$	$\delta$	Mem (M)	$Its_{\text{newton}}$	$Its_{\text{linear}}$	$Its_{\text{sweep}}$	$Time_{\text{low}}(s)$	$Time_{\text{high}}(s)$	$Time_{\tau}(s)$	EFF
160	0	1587	2	32	30	661	626	1287	100%
160	1	2302	2	28	28	636	653	1289	100%
160	2	2680	2	26	25	595	678	1273	100%
320	0	810	2	33	30	348	315	663	97%
320	1	1194	2	28	28	333	336	669	96%
320	2	1422	2	26	25	314	370	684	93%
640	0	427	2	34	30	187	165	352	91%
640	1	656	2	29	29	185	187	372	87%
640	2	798	2	26	26	171	220	391	81%
1,280	0	210	2	35	31	111	89	200	80%
1,280	1	341	2	29	28	106	108	214	75%
1,280	2	526	2	26	26	103	136	239	67%

The neutron transport problem is accelerated by the low order diffusion system. For solving the linear system of equations in the transport system, the preconditioning matrix is coarsened with the subspace-based coarsening algorithm to generate 7 subinterpolations, and a seven-level preconditioner is constructed using these subinterpolations. On the finest level a Schwarz preconditioner with different overlapping sizes is employed, and no overlapping is used on all other coarse levels except the coarsest level on which a direct solver is carried out redundantly. The low order diffusion system is computed with Newton-Krylov-SGMASM with an initial guess obtained from two inverse power iterations. The linear system of transport equations is also solved with SGMASM preconditioned GMRES with a seven-level hierarchy.

In Table 1, it is easily observed that more memory is used as we increase the subdomain overlapping size, especially when  $\delta$  increases from 0 to 1. “ $\delta = 1$ ” uses much more memory than “ $\delta = 0$ ” because the local submatrix with “ $\delta = 0$ ” is implemented in place while the implementation of “ $\delta = 1$ ” has to involve an extra submatrix copy for storing overlapping and local elements. For the 160-core case, the overall algorithm with  $\delta = 0$  consumes 1587 M memory (per

processor core), and the memory usage is increased to 2302 M by 715 M when we increase  $\delta$  to 1. The memory usage continues being increased to 2680 M by 378 M when we continue increasing  $\delta$  to 2. The number of Newton iterations per Picard iteration stays as a constant for all overlapping sizes and all core counts. The number of GMRES iterations per Newton step in the diffusion system decreases slightly when a larger overlapping size is employed so that the compute time on the diffusion system is reduced accordingly. GMRES iteration for the transport system is, similarly, decreased when we change  $\delta$  from 0, to 1 and 2, but the compute time on the transport system does not decrease, instead, it is increased from 626 s, to 653 s and 678 s when 160 processor cores are used because the per-iteration cost with a larger  $\delta$  is higher than that obtained with a smaller  $\delta$ . That is, the reduction in GMRES iteration can not compensate the per-iteration-cost increase. The total compute times with different overlapping sizes at 160 processor cores are close to each other because the time reduction in the diffusion system is cancelled by the time increase in the transport system.

We now try to understand how the overall algorithm performance correlates to the overlapping size when the number of processor cores is increased. The proposed algorithm with  $\delta = 0$  is scalable in memory in the sense that the memory usage is halved when we double the number of processor cores. More precisely, the memory usage with  $\delta = 0$  is almost halved to 810 M from 1587 M when the core count is doubled from 160 to 320. It continues being reduced to 427 M and 210 M, respectively, when the number of processor cores is increased to 640 and 1,280. For both  $\delta = 1$  and 2, we observed the similar behaviors, that is, the overall algorithm equipped with different overlapping sizes is scalable in memory. The memory usages with  $\delta = 1$  and 2 are much higher than that consumed with  $\delta = 0$  for all core counts. At 1,280 processor cores, the memory consumed with  $\delta = 1$  is almost twice as much as that using  $\delta = 0$ . The memory usage using  $\delta = 2$  is 2.5 times as much as that consumed with  $\delta = 0$ . The overall algorithm is mathematically scalable since the averaged numbers of GMRES iterations in both the transport and the diffusion

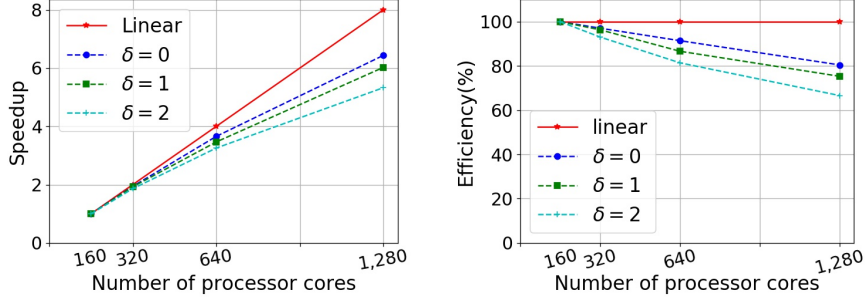


Figure 5: Speedup and efficiency for different overlapping sizes on 160, 320, 640 and 1,280 processor cores. Left: speedup, right: parallel efficiency.

systems stay close to constants for all core counts. The compute times in the diffusion system with  $\delta = 0$  are more than other cases for all core counts, while the algorithm performs better with a smaller overlapping size in the transport system, e.g.,  $\delta = 0$  is better than the nonzero overlapping sizes. We conclude that  $\delta = 0$  is an optimal choice for the transport system, and  $\delta = 2$  is a better choice for the diffusion system. The overall algorithm is highly scalable for different overlapping sizes with up to 1,280 processor cores. Parallel efficiencies of 80%, 75% and 67% are obtained when using  $\delta = 0, 1$  and  $2$  at 1,280 processor cores. The speedups and parallel efficiencies are also shown in Fig. 5, where the algorithm using  $\delta = 0$  is obviously better than all other cases.

To further understand the preconditioner performance, the compute times on the individual components of the diffusion system are reported in Table 2, where the compute times on the preconditioner setup and application increase for all core counts when the overlapping size is increased. The linear solver time is reduced when we increase the overlapping size because the corresponding GMRES iteration is decreased. For example, at 160 processor cores, the linear solver time is decreased from 584 s to 559 s and 518 s when  $\delta$  is increased from 0 to 1 and 2. The compute time on the matrix-free matrix-vector operations is also decreased when we increase the overlapping size, which is observed for all core counts. For instance, at 640 processor cores, the compute

Table 2: Compute times on the individual components of the diffusion system using different overlapping sizes on 160, 320, 640 and 1,280 processor cores.

$np$	$\delta$	Time <sub>ksp</sub> (s)	Time <sub>PCA</sub> (s)	Time <sub>PCS</sub> (s)	Time <sub>MF</sub> (s)	Time <sub>Func</sub> (s)	Time <sub>Jac</sub> (s)	Time <sub>LS</sub> (s)
160	0	584	38	15	547	28	31	37
160	1	559	45	17	514	28	31	37
160	2	518	48	18	470	28	31	36
320	0	307	20	9	286	15	16	19
320	1	293	25	10	267	14	16	19
320	2	274	28	11	245	14	16	19
640	0	167	13	6	151	8	8	10
640	1	164	16	6	145	7	8	10
640	2	150	19	7	130	7	8	10
1,280	0	99	10	6	86	4	4	6
1,280	1	94	13	6	75	4	5	5
1,280	2	92	14	5	75	4	4	5

time on the matrix-free matrix-vector operations is reduced from 151 s to 145 s when  $\delta$  is increased from 0 to 1, and it continues being decreased to 130 s by 15 s with using  $\delta = 2$ . The compute times on the Jacobian evaluations, the function evaluations and the line search are almost the same for different overlapping sizes since the number of Newton iterations stay the same regardless of the overlapping size. In the diffusion system, the matrix-free matrix-vector operations dominate the whole calculations so that a reduction on the matrix-free operations due to a large overlapping size leads to a more efficient computation.

In the transport system, the scattering and the fission terms are computed using the scalar fluxes and the eigenvalue from the diffusion system, and then only a linear system of equations needs to be solved at each Picard iteration. The compute times for the individual components of the transport system are shown in Table 3. We observed that the preconditioner setup time is negligibly increased when using different  $\delta$ , and it takes only a small portion of the total compute time because the preconditioner is fixed in the transport system for the entire simulation so that only one preconditioner setup is involved at



Table 3: Preconditioner performance in the transport system with different overlapping sizes on 160, 320, 640 and 1,280 processor cores.

$np$	$\delta$	Time <sub>PCS</sub> (s)	Time <sub>PCA</sub> (s)	Time <sub>high</sub> (s)
160	0	18	549	626
160	1	21	582	653
160	2	24	611	678
320	0	10	272	315
320	1	12	298	336
320	2	14	335	336
640	0	7	140	352
640	1	7	166	372
640	2	9	199	391
1,280	0	4	73	200
1,280	1	5	95	214
1,280	2	6	123	239

the beginning of the simulation. Most of the compute time in the transport system is spent on applying the preconditioner to the linear system of equations. When we increase the overlapping size, the preconditioner application time is increased for all core counts. For example, at 160 processor cores, the preconditioner application time is increased from 549 s to 582 s by 33 s when  $\delta$  is increased from 0 to 1. It continues being increased to 611 s when  $\delta = 2$ . At 1,280 processor cores, the preconditioner application times are 73 s, 95 s and 123 s for  $\delta = 0, 1$  and 2, respectively. The preconditioner application time at  $\delta = 2$  is almost twice as much as that at  $\delta = 1$ . The overall compute time with  $\delta = 0$ , in the transport system, is better than the other two options.

#### 4.2. Comparison with an unaccelerated transport solver

The multigroup neutron transport equations can be solved directly without a nonlinear diffusion acceleration method (we have done this in our previous work [11, 12]), where a generalized eigenvalue problem instead of a linear system of equations is involved. The goal of the nonlinear diffusion acceleration method is to decouple the fission and the scattering terms from other terms in the transport equations so that only a linear system of equations needs to

Table 4: Performance comparison between the unaccelerated transport solver and the diffusion accelerated transport method using 1,280 processor cores.

$N_d$	algorith	Mem (M)	Time <sub>MF</sub> (s)	Time <sub>PCS</sub> (s)	Time <sub>PCA</sub> (s)	Time <sub>ksp</sub> (s)	Time <sub>T</sub> (s)
32	NDA	212	77	10	88	179	194
32	Unaccelerated	256	246	9	28	283	313
64	NDA	433	71	14	165	261	281
64	Unaccelerated	496	567	16	56	639	705
128	NDA	868	72	20	353	476	502
128	Unaccelerated	985	1241	29	113	1382	1527
192	NDA	1353	75	29	662	833	868
192	Unaccelerated	1423	2204	46	267	2483	2727

be computed, which in turn reduces the computational cost. In this test, we do a performance comparison between the unaccelerated transport solver and the diffusion accelerated transport method. In the diffusion accelerated transport method, “ $\delta = 0$ ” is employed for the transport system and “ $\delta = 2$ ” is adopted for the diffusion system. In the unaccelerated transport solver, an inexact Newton-Krylov method together with SGMASM is used to directly solve the generalized eigenvalue problem. More details on the unaccelerated transport solver can be found in our previous work [12, 24].

The performance comparison between the unaccelerated transport solver and the diffusion accelerated transport method is reported in Table 4. The test is carried out using 1,280 processor cores with different numbers of angular directions. “NDA” represents the nonlinear diffusion accelerated transport solver, and “Unaccelerated” denotes the unaccelerated transport solver.

It is observed, from Table 4, that the memory usage in the unaccelerated transport solver is slightly higher than that in the diffusion accelerated transport method since the diffusion system takes a negligible amount of memory. Take  $N_d = 32$  as an example, where the memory consumed by the diffusion accelerated transport method is less than that used in the unaccelerated transport solver by 44 M. The memory difference between the unaccelerated transport solver and the diffusion accelerated transport algorithm becomes larger

as more angular directions are used. The difference is 63 M at 64 angular directions, and it grows to 117 M and 70 M when 128 and 192 angular directions are employed. The compute time on the matrix-free matrix-vector operations, in the diffusion accelerated transport solver, does not change much as more angular directions are added because the matrix-free matrix-vector operations occur in the low order diffusion system and the diffusion system stays the same regardless of the number of angular directions. On the other hand, the compute time of the matrix-free matrix-vector operations for the unaccelerated transport solver is doubled as we double the number of angular directions since the transport problem becomes twice larger when the number of angular directions is doubled. For instance, the compute time spent on the matrix-free matrix-vector operations is 246 s when using 32 angular directions, and it grows to 567 s, 1241 s and 2204 s for 64, 128 and 192 angular directions, respectively. The preconditioner setup time for the diffusion accelerated transport solver is slightly less than that in the unaccelerated transport solver for 64, 128 and 192 angular directions, and it is almost the same as that of the unaccelerated transport solver at 32 angular directions. The preconditioner application time for the diffusion accelerated transport solver is three times as much as that in the unaccelerated transport solver regardless of the number of angular directions since much more GMRES iterations are required. However, the linear solver time of the diffusion accelerated transport algorithm is much less than that spent on the unaccelerated transport solver. For instance, at 32 angular directions, the unaccelerated transport solver takes 283 s on GMRES, while the diffusion accelerated transport solver costs 179 s on GMRES. The unaccelerated transport solver uses twice compute time as much as the diffusion accelerated transport method for 64 angular directions, and this ratio is increased to 3 for 128 and 192 angular directions. For the overall simulation time, the diffusion accelerated transport solver is twice as fast as the unaccelerated transport solver for 32 and 64 angular directions, and it is three times faster for 128 and 192 angular directions. We conclude that the nonlinear diffusion acceleration technique together with SGMASM enhances the transport

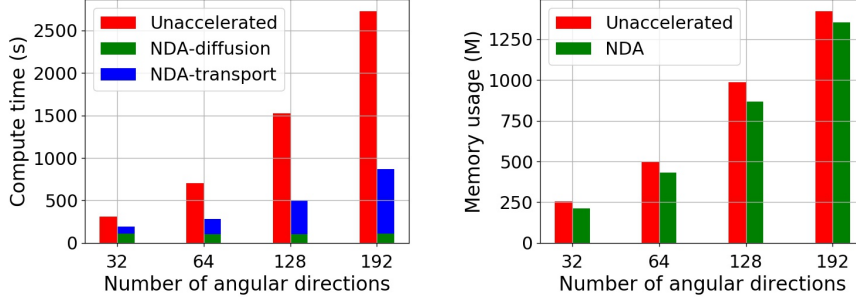


Figure 6: Performance comparison in the compute time and the memory usage with an unaccelerated transport solver using different numbers of angular directions. Right: total compute time; left: memory usage.

criticality calculations significantly.

The performance comparison in the compute time and the memory usage is also drawn in Fig. 6. Here “NDA-diffusion” denotes the low order diffusion system, and “NDA-transport” represents the transport system. It is obvious that the compute time used in the unaccelerated transport solver is much higher than that in the diffusion accelerated transport algorithm especially when the number of angular directions is large. For example, the diffusion accelerated transport solver is three times as fast as the unaccelerated transport solver when using 192 angular directions. The memory usages are similar to each other, and the memory usage in the unaccelerated transport solver is slightly higher than that in the diffusion accelerated transport algorithm.

The compute times on the individual components of the low-order diffusion system are also reported in Table 5 for different numbers of angular directions using 1,280 processor cores. As expected, the compute times on the individual components stay close to constants when we increase the number of angular directions.

The trend does not hold for the transport system as shown in Table 6. Here the averaged number of GMRES iterations per Picard iteration stay close to a constant as more angular directions are used, which indicates that SGMASM

Table 5: Compute times on the individual components of the low-order diffusion system for different numbers of angular directions using 1,280 processor cores.

$N_d$	Time <sub>ksp</sub> (s)	Time <sub>PCA</sub> (s)	Time <sub>PCS</sub> (s)	Time <sub>MF</sub> (s)	Time <sub>Func</sub> (s)	Time <sub>Jac</sub> (s)	Time <sub>LS</sub> (s)	Time <sub>low</sub> (s)
32	95	15	6	77	4	4	6	106
64	89	15	6	71	4	4	6	101
128	95	15	6	72	4	4	6	102
192	97	20	6	75	4	5	6	109

Table 6: Compute times on the preconditioner setup and application of the transport system for different numbers of angular directions using 1,280 processor cores.

$N_d$	Itsweep	Time <sub>PCS</sub> (s)	Time <sub>PCA</sub> (s)	Time <sub>high</sub> (s)
32	35	4	73	88
64	36	8	150	180
128	39	14	338	400
192	39	23	642	759

is scalable in problem size. The compute times on the individual components such as the preconditioner setup and the preconditioner application are doubled as expected when the number of angular directions are doubled. We conclude that the diffusion accelerated transport solver equipped with SGMASM is linearly scalable in problem size.

#### 4.3. Influences of coarsening threshold

In the matrix coarsening algorithm, there is a critical parameter that impacts not only the operator complexity but also the convergence rate. The parameter denoted as “threshold” determines which elements are important to be kept in the strength matrix and which elements can be ignored. More precisely, a connection from  $i$  to  $j$  is included in the strength graph if and only if

$$-\mathbf{M}(i, j) > \theta \max_{k \neq i}(-\mathbf{M}(i, k)).$$

Here  $\mathbf{M}(i, j)$  is the  $j$ th column of the  $i$ th row. If  $\theta$  is too small, the operator complexity will be too high since all connections are considered. If  $\theta$  is too large, the algorithm will not converge since there are not enough coarse points

Table 7: Impacts of coarsening threshold on the algorithm performance using 160, 320, 640 and 1,280 processor cores.

$np$	$\theta$	Mem (M)	$Its_{\text{newton}}$	$Its_{\text{linear}}$	$Its_{\text{sweep}}$	Time <sub>low</sub> (s)	Time <sub>high</sub> (s)	Time <sub><math>\tau</math></sub> (s)	EFF
160	0.25	1587	2	32	30	663	627	1290	66%
160	0.5	1526	2	25	19	445	469	914	93%
160	0.75	1408	2	21	19	452	399	851	100%
160	0.85	1385	2	22	19	462	412	874	97%
320	0.25	810	2	33	30	350	314	664	64%
320	0.5	796	2	25	19	234	241	475	90%
320	0.75	728	2	21	19	236	202	438	97%
320	0.85	742	2	23	19	241	209	450	95%
640	0.25	427	2	34	30	190	164	354	60%
640	0.5	408	2	26	19	129	128	257	83%
640	0.75	380	2	22	19	131	107	238	89%
640	0.85	400	2	23	20	134	112	246	86%
1,280	0.25	210	2	35	31	111	89	200	53%
1,280	0.5	216	2	27	19	83	73	156	68%
1,280	0.75	211	2	23	19	83	60	143	74%
1,280	0.85	210	2	24	20	84	61	145	73%

to resolve low frequency modes. An optimal choice of  $\theta$  is often problem dependent. In [34],  $\theta = 0.25$  is recommended for 2D elliptic problems and  $\theta = 0.5$  for 3D problems. The coarsening threshold is introduced to construct strength matrices where only important coefficients should be kept.

In this test, we study the algorithm performance with respect to  $\theta$  on different numbers of processor cores. The same configuration as before is employed, and the numerical results are reported in Table 7. It is easily observed, from Table 7, that the number of Newton iterations stays as a constant for all values of  $\theta$  for all core counts. The memory usage often decreases as a larger  $\theta$  is used. For example, at 160 processor cores, the memory usage reduces from 1587 M to 1526 M by 61 M when  $\theta$  is increased from 0.25 to 0.5. It continues being reduced to 1408 M and 1385 M, when  $\theta = 0.75$  and  $\theta = 0.85$ , respectively. The same behaviors are observed for high core counts as well; e.g., at 640 processor cores, the memory consumption becomes small to 408 M and 380 M from 427 M as  $\theta$  grows from 0.25 to 0.5 and 0.75. It is because the operator complex-

ity is reduced when a larger threshold is employed. There are some exceptions where the memory usage is increased as a larger  $\theta$  is used because the averaged number of GMRES iterations in the diffusion system or the transport system or both becomes larger. The averaged number of GMRES iterations in the diffusion system becomes smaller at the beginning when we increase  $\theta$  from 0.25 to 0.5, and then it does not change much any more when we keep increasing  $\theta$ . For the 160-core case, the averaged number of GMRES iterations for the diffusion system at  $\theta = 0.25$  is 32, and it is reduced to 25 by 7 at  $\theta = 0.5$ , and to 21 at  $\theta = 0.75$ , but it is increased by one iteration at  $\theta = 0.85$ , which indicates that  $\theta = 0.85$  is too big for this particular problem. Compared with the diffusion system, the threshold has a bigger impact on the the transport system. The averaged number of GMRES iterations per Picard iteration is almost halved when  $\theta = 0.5$  is used instead of  $\theta = 0.25$ ; e.g., the number of GMRES iterations is decreased from 30 to 19 at 160 processor cores as  $\theta$  is increased from 0.25 to 0.5. It is kept close to constants for  $\theta = 0.5, 0.75$  and 0.85. The compute time in both the diffusion and the transport systems decreases significantly at the beginning, and then does not change much. This trend is consistent with the number of GMRES iterations. Take the 160-core case as an example, where the compute time in the diffusion system is reduced from 663 s to 445 s by 218 s when we increase the threshold from 0.25 to 0.5, and then it does not change much for  $\theta = 0.75$  and 0.85. The transport system has a similar trend, that is, it is decreased from 627 s to 469 s by 160 s as  $\theta$  is increased from 0.25 to 0.5 and does not change much for  $\theta = 0.75$  and  $\theta = 0.85$ . The total simulation time has exactly the same trend as the compute times on the diffusion system and the transport system because it is a simple summation of the compute times of both. The parallel efficiency is computed using the smallest compute time obtained at 160 cores as a base so that a higher efficiency represents a more efficient simulation.  $\theta = 0.25$  has a relatively low parallel efficiency, and all other choices have good parallel efficiencies. Even with up to 1,280 processor cores, the proposed algorithm is able to maintain a parallel efficiency above or around 70%. The proposed algorithm equipped with  $\theta = 0.75$  has the best

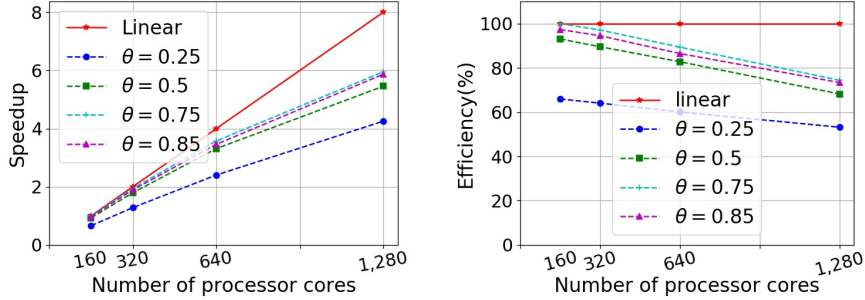


Figure 7: Speedup and parallel efficiency for different coarsening thresholds on 160, 320, 640 and 1,280 processor cores.

performance, and it has a parallel efficiency as high as 74% on 1,280 processor cores. The speedup and parallel efficiency are also drawn in Fig. 7, where we observe that  $\theta = 0.75$  is always better than the other choices.

To further understand the influences of coarsening thresholds, the compute times on the individual components of the diffusion system are summarized in Table 8. It is found that the compute time on the linear solver decreases significantly as  $\theta$  is increased from 0.25 to 0.5, and it stays close to constants for  $\theta = 0.75$  and  $\theta = 0.85$ , which is consistent with the number of GMRES iterations. The preconditioner setup times are almost the same for all cases, and the preconditioner application time has a similar trend as the linear solver time, that is, it decreases at the beginning and then does not change much. As expected, the compute times on the line search operations, the function evaluations and the Jacobian evaluations stay the same for all values of  $\theta$  because they are determined by the number of Newton iterations that is a constant for all cases. The compute time on the matrix-free matrix-vector operations is completely determined by the number of GMRES iterations so that it has the same trend as the number of GMRES iterations. For instance, at 640 processor cores, the compute time of the matrix-free operations is reduced from 152 s to 93 s by 40%, and it does not change much for  $\theta = 0.75$  and 0.85.  $\theta = 0.75$  is the best choice in the diffusion system in the sense that the compute time is the



Table 8: Compute times on the individual components of the diffusion system with respect to different coarsening thresholds using 160, 320, 640, and 1,280 processor cores.

$np$	$\theta$	Time <sub>ksp</sub>	Time <sub>PCS</sub> (s)	Time <sub>PCA</sub> (s)	Time <sub>MF</sub> (s)	Time <sub>Func</sub> (s)	Time <sub>Jac</sub> (s)	Time <sub>LS</sub> (s)
160	0.25	585	15	39	548	28	31	37
160	0.5	368	11	28	347	28	31	37
160	0.75	374	11	30	371	28	31	37
160	0.85	384	10	30	362	28	31	37
320	0.25	310	9	21	289	15	16	19
320	0.5	194	7	16	180	15	16	19
320	0.75	196	7	17	181	15	16	19
320	0.85	201	7	17	186	14	16	19
640	0.25	170	7	15	152	7	8	10
640	0.5	108	7	13	93	8	8	10
640	0.75	110	6	13	95	8	8	10
640	0.85	113	5	14	98	8	8	10
1,280	0.25	100	6	10	86	4	4	5
1,280	0.5	71	8	14	53	4	4	6
1,280	0.75	71	6	14	54	4	4	6
1,280	0.85	72	7	13	55	4	5	6

smallest.

Similarly, the compute times on the individual components of the transport system are also drawn in Table 9. Here the preconditioner setup time is almost the same for all coarsening thresholds except at 160 processor cores, where  $\theta = 0.25$  takes 50% more compute time than that using other thresholds. The preconditioner application time decreases a lot as  $\theta$  is increased from 0.25 to 0.5, and it slightly decreases again when using  $\theta = 0.75$ , and then it becomes a little larger for  $\theta = 0.85$ . For the 160-core case, the preconditioner application time is reduced from 549 s to 417 s by 24% as  $\theta$  grows from 0.25 to 0.5, and it continues being reduced to 354 s by 15% when  $\theta = 0.75$ , and then it slightly increases to 365 s for  $\theta = 0.85$ . This trend holds for all core counts. The total compute time of the transport system behaves in the same way as the preconditioner application time because the preconditioner application accounts for 90% of the total compute time. Again,  $\theta = 0.75$  is the best choice in terms of the compute time for the transport system.

Table 9: Compute times on the individual components of the transport system using different coarsening thresholds on 160, 320, 640, and 1,280 processor cores.

$np$	$\theta$	Time <sub>PCS</sub> (s)	Time <sub>PCA</sub> (s)	Time <sub>high</sub> (s)
160	0.25	18	549	627
160	0.5	13	417	469
160	0.75	12	354	399
160	0.85	11	365	412
320	0.25	10	273	314
320	0.5	8	211	241
320	0.75	7	177	202
320	0.85	7	184	209
640	0.25	6	140	164
640	0.5	5	110	128
640	0.75	5	93	107
640	0.75	4	96	112
1,280	0.25	4	74	89
1,280	0.5	5	61	73
1,280	0.75	3	51	60
1,280	0.85	3	51	61

#### 4.4. Influences of the number of aggressive coarsening levels

The complexity of coarse operators affects the algorithm performance in the memory usage and the compute time. A high-complexity coarse operator uses more memory and costs more compute time per iteration. The complexity of coarse operators can be reduced by introducing an aggressive coarsening scheme whose basic idea is to keep as few coarse points as possible in the coarse levels [12, 34].

In this test, we study the influences of the numbers of aggressive coarsening levels on the complexity of the coarse operators and on the algorithm performance. The same configuration as before is used. “agg=0” denotes that no aggressive coarsening is applied. The numerical results are summarized in Table 10.

It is found, from Table 10, that the memory usage becomes smaller as more aggressive coarsening levels are employed. For the 160-core case, the memory usage is reduced by 23% from 2136 M to 1627 M when one aggressive coars-

Table 10: Influences of the number of aggressive coarsening levels on the algorithm performance using 160, 320, 640 and 1,280 processor cores.

$np$	agg	Mem (M)	Comp	$Its_{linear}$	$Its_{sweep}$	Time <sub>low</sub> (s)	Time <sub>high</sub> (s)	Time <sub>T</sub> (s)	EFF
160	0	2136	2.77	16	17	459	508	967	88%
160	1	1627	1.88	20	18	449	452	901	94%
160	2	1475	1.64	21	18	446	416	862	99%
160	4	1414	1.55	21	19	454	401	862	99%
160	8	1408	1.55	21	19	451	399	850	100%
320	0	1057	2.79	17	17	247	263	510	83%
320	1	864	1.89	20	18	245	230	475	89%
320	2	755	1.65	21	18	246	213	459	93%
320	4	730	1.56	22	19	242	203	445	96%
320	8	728	1.55	22	19	239	200	439	97%
640	0	542	2.83	17	17	141	142	283	75%
640	1	431	1.92	21	18	145	126	271	78%
640	2	409	1.66	22	18	140	116	256	83%
640	4	383	1.57	22	19	135	109	244	87%
640	8	380	1.56	22	19	129	107	236	90%
1,280	0	303	2.86	18	17	99	81	180	59%
1,280	1	239	1.95	22	18	96	73	169	63%
1,280	2	230	1.67	23	18	89	66	155	69%
1,280	4	212	1.57	23	19	87	62	149	71%
1,280	8	211	1.57	23	19	80	61	141	75%

ening level is introduced. It continues being decreased to 1475 M by 9% and to 1414 M by 4% as 2 and 4 aggressive coarsening levels are used, respectively, and it stays almost the same for “agg=8”. The same pattern is observed for all other core counts, that is, the memory usage is reduced significantly for “agg=1” and “agg=2”, and stays almost the same for “agg=4” and “agg=8”. This pattern occurs because of the complexity of the coarse operators. The complexity drops much when “agg=1” is employed instead of “agg=0”. For example, at 1,280 processor cores, the complexity is reduced from 2.86 to 1.95 by 31% when “agg=1” is used, and continues becoming a little smaller as “agg=2”, “agg=4” and “agg=8” are adopted. We do not list the number of Newton iterations since it is kept as a constant, 2, for all cases. The number of GMRES iterations in the diffusion system becomes larger as more aggressive coarsening levels are used, but the performance of the resulting algorithm does not deteriorate because the per-iteration cost decreases significantly. The number of GMRES iterations in the transport system stays close to constants for different numbers of aggressive coarsening levels. The number of aggressive coarsening levels does not influence the compute time much in the diffusion system when the number of processor cores is small, but it has a bigger impact when we use more cores. For example, the compute time of the diffusion system is reduced to 80 s from 99 s by 20% when “agg=8” is employed. On the other hand, the number of aggressive coarsening levels has a consistent impact on the algorithm performance for the transport system. More precisely, as “agg=8” is employed the compute time is reduced by 25% - 30%. For example, for the 320-core case, the compute time in the transport system reduces from 263 s to 230 s, 213 s, 203 s and 200 s when the number of aggressive coarsening levels is increased from 0 to 1, 2, 4 and 8. The compute time at ‘agg=8’ is 24% less than that using “agg=0”. The total compute time correlates to the complexity of the coarse operators, that is, it decreases at the beginning and then does not change much. The parallel efficiency is computed using the smallest compute time obtained with 160 processor cores as a base. The proposed algorithm with “agg=8” has the best parallel efficiency, and a parallel efficiency as high as 75%

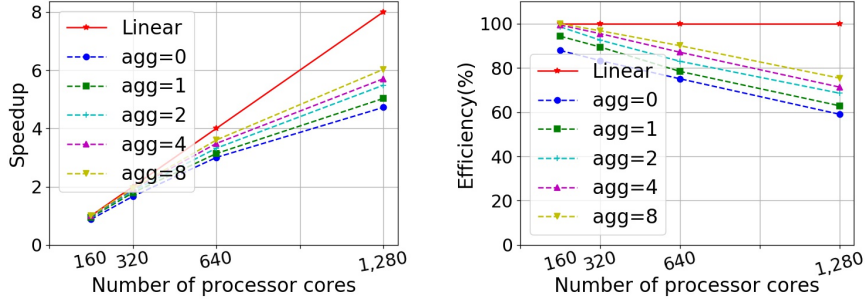


Figure 8: Speedup and parallel efficiency for different numbers of aggressive coarsening levels on 160, 320, 640 and 1,280 processor cores. Left: speedup; right: parallel efficiency.

is obtained with up to 1,280 processor cores.

The speedup and the parallel efficiency are also drawn in Fig. 8, where we found that a larger number of aggressive coarsening levels often leads to a better parallel efficiency for all core counts.

We next study the impacts of the number of aggressive coarse levels on the individual components of the diffusion system. The compute times on the individual components of the diffusion system using different numbers of aggressive coarse levels are reported in Table 11. As more processor cores are used, the impacts of the number of aggressive coarsening levels on the linear solver time become larger. When using 160 processor cores, the compute time on the linear solver in the diffusion system does not change much with an increase in the number of aggressive coarsening levels, while the linear solver time obtained using “agg=8” is 22% less than that with “agg=0” when the number of processor cores is 1,280. The preconditioner setup time is reduced significantly when the number of aggressive coarsening levels is increased from 0 to 1, and then continues gradually decreasing for “agg=2”, “agg=4” and “agg=8”. Take the 1,280-core case as an example, where the preconditioner setup time is reduced by 50% from 11 s to 6 s when “agg=8” is employed instead of “agg=0”. This pattern is shown for the preconditioner application time as well. It decreases much when one aggressive coarsening level is adopted, and slightly

Table 11: Compute times on the individual components of the diffusion system with respect to different numbers of aggressive coarsening levels using 160, 320, 640 and 1280 processor cores.

$np$	agg	Time <sub>ksp</sub> (s)	Time <sub>PCS</sub> (s)	Time <sub>PCA</sub> (s)	Time <sub>MF</sub> (s)	Time <sub>Func</sub> (s)	Time <sub>Jac</sub> (s)	Time <sub>LS</sub> (s)
160	0	380	25	53	320	28	31	37
160	1	371	17	40	332	28	31	37
160	2	369	14	38	335	28	31	37
160	4	376	12	34	348	28	31	37
160	8	373	11	30	350	28	31	37
320	0	206	17	35	163	15	16	19
320	1	245	11	29	173	14	16	19
320	2	206	10	27	177	15	16	19
320	4	202	8	22	181	15	16	19
320	8	198	8	18	182	14	17	19
640	0	120	12	27	85	8	8	10
640	1	123	9	25	93	8	9	10
640	2	119	8	23	92	8	8	10
640	4	114	6	18	94	7	8	10
640	8	108	6	12	94	8	8	10
1,280	0	88	11	29	49	4	5	6
1,280	1	85	9	27	50	4	4	6
1,280	2	78	7	22	51	4	4	6
1,280	4	75	7	17	54	4	5	6
1,280	8	69	6	12	54	4	4	5

reduces as more aggressive levels are used. For example, for the 320-core case, the preconditioner application time reduces to 29 s from 35 s when the number of aggressive coarsening levels is increased from 0 to 1, and continues being decreased to 27 s , 22 s and 18 s when the number of aggressive coarsening levels is increased to 2, 4 and 8. The compute time on the matrix-free operations is increased as more aggressive coarsening levels are used because the resulting algorithm has more GMRES iterations. However, the time increase on the matrix-free operations is compensated by the time reduction on the preconditioner setup and application so that the total compute time is properly decreased as more aggressive coarsening levels are employed. The compute times on the Jacobian evaluations, the function evaluations and the line search are almost exactly the same for all cases since they are determined by the number of Newton iterations that is the same for all tests.

Similarly, we report the compute times on the individual components of the transport system in Table 12. The same pattern observed earlier presents in the transport system. More precisely, the preconditioner setup time for the transport system decreases much at the beginning, and then gradually decreases as more aggressive coarsening levels are used. For example, at 640 processor cores, the preconditioner setup takes 11 s when “agg=0”, and the compute time is halved to 5 s when the number of aggressive coarsening levels is 8. Similarly, the preconditioner application time and the total compute time decrease as we employ more aggressive coarsening levels. We conclude that in this test “agg=8” is the best in terms of the memory usage and the compute time for the overall simulation. A large number of aggressive coarsening levels are required to maintain a good scalability.

#### *4.5. Comparison with a traditional multilevel method*

In this test, we compare the performance of the monolithic multilevel method equipped with the subspace- based coarsening algorithm with that of the unmodified traditional multilevel method using the full space based coarsening approach. The subspace-based coarsening algorithm mainly aims at reducing

Table 12: Compute times on the individual components of the transport system using different numbers of aggressive coarsening levels on 160, 320, 640 and 1,280 processor cores.

$np$	agg	Time <sub>PCS</sub> (s)	Time <sub>PCA</sub> (s)	Time <sub>high</sub> (s)
160	0	28	457	508
160	1	18	403	452
160	2	14	369	416
160	4	12	356	401
160	8	12	353	399
320	0	17	233	263
320	1	11	202	230
320	2	9	187	213
320	4	7	179	203
320	8	7	178	200
640	0	11	123	142
640	1	7	110	126
640	2	6	100	116
640	4	5	94	109
640	8	5	93	107
1,280	0	7	70	81
1,280	1	6	61	73
1,280	2	4	56	66
1,280	4	3	53	62
1,280	8	4	50	61



Table 13: Performance comparison between SGMASM and MASM using up to 5,120 processor cores.

$np$	Algorithm	Time <sub>PCS</sub> (s)	Time <sub>PCA</sub> (s)	Time <sub>MF</sub> (s)	Time <sub>Func</sub> (s)	Time <sub>T</sub> (s)	EFF
1,280	SGMASM	47	1171	391	29	1802	100%
1,280	MASM	–	–	–	–	–	–
2,560	SGMASM	41	751	207	15	1105	82%
2,560	MASM	401	1020	250	19	1700	53%
5,120	SGMASM	28	476	160	11	734	61%
5,120	MASM	251	920	136	10	1362	33%

the preconditioner setup cost, and meanwhile is able to improve the preconditioner application performance. The mesh used in this test is finer than that in the previous tests since more processor cores will be used. The mesh has 6,464,825 nodes and 12,543,552 elements. The diffusion system has 45,253,775 unknowns, and the transport system has 2,896,241,600 unknowns with 64 angular directions. The numerical results are summarized in Table 13.

It is found that the preconditioner setup time is significantly reduced by using SGMASM. The data misses for MASM at 1,280 processor cores because MASM requires the amount of memory beyond the machine memory limit. For 2,560 and 5,120 processor cores, the preconditioner setup of SGMASM is ten times as fast as that of MASM. The preconditioner setup of MASM takes 401 s at 2,560 processor cores and 251 s at 5,120 processor cores, while that of SGMASM costs only 41 s and 28 s, respectively. The preconditioner application is improved by a factor of 2, compared with MASM. The preconditioner application time obtained using MASM is twice as high as that used by SGMASM, that is, SGMASM is once faster than MASM in the preconditioner application for 2,560 and 5,120 processor cores. The compute times on the matrix-free operations are similar to each other for all core counts. Similarly, the compute times on the function evaluations are close to each other. For the overall simulation, SGMASM is able to run once faster than MASM. SGMASM is capable of maintaining a good parallel efficiency with up to 5,120 processor cores, while MASM is inefficient.

## 5. Concluding remarks

A nonlinear diffusion acceleration method has been studied to improve the transport criticality calculations, where the scattering and fission terms are evaluated using the computed scalar fluxes and eigenvalue from the nonlinear diffusion equations. To compute the eigenvalue of the low order diffusion system, an inexact Jacobian-free Newton with a few inverse power iterations as an initial guess was employed, and during each Newton iteration a parallel monolithic multilevel preconditioner together with GMRES was adopted for calculating the Jacobian system. The monolithic multilevel method was also used for the solution of the linear system of transport equations. To reduce the cost on the coarse space construction of the multilevel method, we studied a subspace-based coarsening algorithm that has been shown to be more efficient than a traditional full-space coarsening approach on thousands of processor cores for an unstructured mesh problem with billions of unknowns. We have numerically verified that the overall algorithm equipped with several important ingredients; e.g., subspace-based coarsening, monolithic coupling, strength matrix thresholding and aggressive coarsening, is scalable with up to thousands of processor cores.

While this work focuses on a multilevel Schwarz preconditioner for accelerating neutron transport calculations, other techniques such as Method of Characteristics (MOC) [10, 56] may be explored in the future. Only strong scaling results were reported in this work, and weak scaling will be explored in our future work.

## Acknowledgments

This manuscript has been authored by Battelle Energy Alliance, LLC under Contract No. DE-AC07-05ID14517 with the U.S. Department of Energy. The United States Government retains and the publisher, by accepting the article for publication, acknowledges that the United States Government retains

a nonexclusive, paid-up, irrevocable, world-wide license to publish or reproduce the published form of this manuscript, or allow others to do so, for United States Government purposes.

This research made use of the resources of the High-Performance Computing Center at Idaho National Laboratory, which is supported by the Office of Nuclear Energy of the U.S. Department of Energy and the Nuclear Science User Facilities under Contract No. DE-AC07-05ID14517.

## References

- [1] E. E. Lewis, W. F. Miller, *Computational Methods of Neutron Transport*, John Wiley and Sons Inc., New York, NY, 1984.
- [2] J. J. Duderstadt, *Nuclear Reactor Analysis*, Wiley, Hoboken, NJ, 1976.
- [3] D. Kaushik, M. Smith, A. Wollaber, B. Smith, A. Siegel, W. S. Yang, Enabling high-fidelity neutron transport simulations on petascale architectures, in: *Proceedings of the Conference on High Performance Computing Networking, Storage and Analysis, SC '09*, ACM, New York, NY, USA, 2009, pp. 67:1–67:12. doi:10.1145/1654059.1654128.  
URL <http://doi.acm.org/10.1145/1654059.1654128>
- [4] A. J. Kunen, T. S. Bailey, P. N. Brown, KRIPKE- A massively parallel transport mini-app, Tech. rep., Lawrence Livermore National Lab. (LLNL), Livermore, CA (United States) (2015).
- [5] G. G. Davidson, T. M. Evans, J. J. Jarrell, S. P. Hamilton, T. M. Pandya, R. N. Slaybaugh, Massively parallel, three-dimensional transport solutions for the k-eigenvalue problem, *Nuclear Science and Engineering* 177 (2) (2014) 111–125.
- [6] Y. Saad, *Numerical Methods for Large Eigenvalue Problems: Revised Edition*, Vol. 66, SIAM, Philadelphia, PA, 2011.

- [7] R. E. Alcouffe, Diffusion synthetic acceleration methods for the diamond-differenced discrete-ordinates equations, *Nuclear Science and Engineering* 64 (2) (1977) 344–355.
- [8] K. S. Smith, Full-core, 2-D, LWR core calculations with CASMO-4E, in: *Proceedings of PHYSOR 2002*, 2002.
- [9] S. Schunert, Y. Wang, F. Gleicher, J. Ortensi, B. Baker, V. Laboure, C. Wang, M. DeHart, R. Martineau, A flexible nonlinear diffusion acceleration method for the SN transport equations discretized with discontinuous finite elements, *Journal of Computational Physics* 338 (2017) 107–136.
- [10] S. Shaner, G. Gunow, F. Benoit, K. Smith, Verification of the 3D method of characteristics solver in OpenMOC.
- [11] F. Kong, Y. Wang, D. R. Gaston, A. D. Lindsay, C. J. Permann, R. C. Martineau, A scalable multilevel domain decomposition preconditioner with a subspace-based coarsening algorithm for the neutron transport calculations, *arXiv preprint arXiv:1906.07743*, 2019.
- [12] F. Kong, Y. Wang, D. R. Gaston, C. J. Permann, A. E. Slaughter, A. D. Lindsay, R. C. Martineau, A highly parallel multilevel Newton-Krylov-Schwarz method with subspace-based coarsening and partition-based balancing for the multigroup neutron transport equations on 3D unstructured meshes, *arXiv preprint arXiv:1903.03659*, 2019.
- [13] G. Kanschat, J.-C. Ragusa, A robust multigrid preconditioner for SN DG approximation of monochromatic, isotropic radiation transport problems, *SIAM Journal on Scientific Computing* 36 (5) (2014) A2326–A2345.
- [14] B. Chang, T. Manteuffel, S. McCormick, J. Ruge, B. Sheehan, Spatial multigrid for isotropic neutron transport, *SIAM Journal on Scientific Computing* 29 (5) (2007) 1900–1917.

- [15] T. Manteuffel, S. McCormick, J. Morel, S. Oliveira, G. Yang, A fast multi-grid algorithm for isotropic transport problems I: Pure scattering, *SIAM Journal on Scientific Computing* 16 (3) (1995) 601–635.
- [16] S. Balay, S. Abhyankar, M. F. Adams, J. Brown, P. Brune, K. Buschelman, L. Dalcin, A. Dener, V. Eijkhout, W. D. Gropp, D. Karpeyev, D. Kaushik, M. G. Knepley, D. A. May, L. C. McInnes, R. T. Mills, T. Munson, K. Rupp, P. Sanan, B. F. Smith, S. Zampini, H. Zhang, H. Zhang, *PETSc Users Manual*, Tech. Rep. ANL-95/11 - Revision 3.11, Argonne National Laboratory (2019).  
URL <https://www.mcs.anl.gov/petsc>
- [17] H. Zhang, R. T. Mills, K. Rupp, B. F. Smith, Vectorized parallel sparse matrix-vector multiplication in PETSc using AVX-512, in: *Proceedings of the 47th International Conference on Parallel Processing*, ACM, 2018, p. 55.
- [18] B. C. Yee, B. Kochunas, E. W. Larsen, Y. Xu, Space-dependent Wielandt shifts for multigroup diffusion eigenvalue problems, *Nuclear Science and Engineering* 188 (2) (2017) 140–159.
- [19] R. S. Dembo, S. C. Eisenstat, T. Steihaug, Inexact Newton methods, *SIAM Journal on Numerical analysis* 19 (2) (1982) 400–408.
- [20] D. A. Knoll, D. E. Keyes, Jacobian-free Newton–Krylov methods: A survey of approaches and applications, *Journal of Computational Physics* 193 (2) (2004) 357–397.
- [21] D. Knoll, H. Park, C. Newman, Acceleration of k-eigenvalue/criticality calculations using the Jacobian-free Newton-Krylov method, *Nuclear Science and Engineering* 167 (2) (2011) 133–140.
- [22] D. F. Gill, Y. Y. Azmy, J. S. Warsa, J. D. Densmore, Newton’s method for the computation of k-eigenvalues in SN transport applications, *Nuclear Science and Engineering* 168 (1) (2011) 37–58.

- [23] M. T. Calef, E. D. Fichtl, J. S. Warsa, M. Berndt, N. N. Carlson, Nonlinear Krylov acceleration applied to a discrete ordinates formulation of the k-eigenvalue problem, *Journal of Computational Physics* 238 (2013) 188–209.
- [24] F. Kong, Y. Wang, S. Schunert, J. W. Peterson, C. J. Permann, D. Andrš, R. C. Martineau, A fully coupled two-level Schwarz preconditioner based on smoothed aggregation for the transient multigroup neutron diffusion equations, *Numerical Linear Algebra with Applications* 25 (3) (2018) 21–62.
- [25] Y. Wang, S. Schunert, V. Laboure, Rattlesnake Theory Manual, Tech. rep., Idaho National Lab.(INL), Idaho Falls, ID (United States) (2018).
- [26] K. S. Smith, Nodal method storage reduction by nonlinear iteration, *Transactions of the American Nuclear Society* 44 (1983) 265–266.
- [27] L. R. Cornejo, D. Y. Anistratov, Nonlinear diffusion acceleration method with multigrid in energy for k-eigenvalue neutron transport problems, *Nuclear Science and Engineering* 184 (4) (2016) 514–526.
- [28] L. R. Cornejo, D. Y. Anistratov, K. Smith, Iteration methods with multigrid in energy for eigenvalue neutron diffusion problems, *Nuclear Science and Engineering* (2019) 1–25.
- [29] R. Slaybaugh, T. M. Evans, G. G. Davidson, P. P. Wilson, Multigrid in energy preconditioner for Krylov solvers, *Journal of Computational Physics* 242 (2013) 405–419.
- [30] B. C. Yee, B. Kochunas, E. W. Larsen, A multilevel in space and energy solver for multigroup diffusion eigenvalue problems, *Nuclear Engineering and Technology* 49 (6) (2017) 1125–1134.
- [31] B. C. Yee, B. Kochunas, E. W. Larsen, A multilevel in space and energy solver for 3-D multigroup diffusion and coarse-mesh finite difference eigenvalue problems, *Nuclear Science and Engineering* (2019) 1–24.

- [32] F. Kong, X.-C. Cai, A highly scalable multilevel Schwarz method with boundary geometry preserving coarse spaces for 3D elasticity problems on domains with complex geometry, *SIAM Journal on Scientific Computing* 38 (2) (2016) C73–C95.
- [33] F. Kong, X.-C. Cai, A scalable nonlinear fluid–structure interaction solver based on a Schwarz preconditioner with isogeometric unstructured coarse spaces in 3D, *Journal of Computational Physics* 340 (2017) 498–518.
- [34] V. E. Henson, U. M. Yang, BoomerAMG: A parallel algebraic multigrid solver and preconditioner, *Applied Numerical Mathematics* 41 (1) (2002) 155–177.
- [35] J. Morel, J. McGhee, A self-adjoint angular flux equation, *Nuclear Science and Engineering* 132 (3) (1999) 312–325.
- [36] J. L. Liscum-Powell, A. B. Prinja, J. E. Morel, L. J. Lorence Jr, Finite element solution of the self-adjoint angular flux equation for coupled electron-photon transport, *Nuclear science and engineering* 142 (3) (2002) 270–291.
- [37] A. N. Brooks, T. J. Hughes, Streamline upwind/Petrov-Galerkin formulations for convection dominated flows with particular emphasis on the incompressible Navier-Stokes equations, *Computer Methods in Applied Mechanics and Engineering* 32 (1-3) (1982) 199–259.
- [38] J. E. Dennis Jr, R. B. Schnabel, *Numerical Methods for Unconstrained Optimization and Nonlinear Equations*, Vol. 16, SIAM, Philadelphia, PA, 1996.
- [39] M. Pernice, H. F. Walker, NITSOL: A Newton iterative solver for nonlinear systems, *SIAM Journal on Scientific Computing* 19 (1) (1998) 302–318.
- [40] F. Kong, V. Kheifets, E. Finol, X.-C. Cai, An efficient parallel simulation of unsteady blood flows in patient-specific pulmonary artery, *International Journal for Numerical Methods in Biomedical Engineering* 34 (4) (2018)

e2952.

URL <https://doi.org/10.1002/cnm.2952>

- [41] F. Kong, X.-C. Cai, Scalability study of an implicit solver for coupled fluid-structure interaction problems on unstructured meshes in 3D, *The International Journal of High Performance Computing Applications* 32 (2) (2018) 207–219.
- [42] F. Kong, A Parallel Implicit Fluid-structure Interaction Solver with Isogeometric Coarse Spaces for 3D Unstructured Mesh Problems with Complex Geometry, Ph.D. thesis, University of Colorado Boulder, Boulder, CO (2016).
- [43] F. Kong, V. Kheyfets, E. Finol, X.-C. Cai, Simulation of unsteady blood flows in a patient-specific compliant pulmonary artery with a highly parallel monolithically coupled fluid-structure interaction algorithm, *International Journal for Numerical Methods in Biomedical Engineering* 35 (2019) e3208.  
URL <https://doi.org/10.1002/cnm.3208>
- [44] Y. Saad, M. H. Schultz, GMRES: A generalized minimal residual algorithm for solving nonsymmetric linear systems, *SIAM Journal on Scientific and Statistical Computing* 7 (3) (1986) 856–869.
- [45] Y. Saad, *Iterative Methods for Sparse Linear Systems*, Vol. 82, SIAM, 2003.
- [46] C. J. Permann, D. R. Gaston, D. Andrs, R. W. Carlsen, F. Kong, A. D. Lindsay, J. M. Miller, J. W. Peterson, A. E. Slaughter, R. H. Stogner, et al., MOOSE: Enabling massively parallel multiphysics simulation, arXiv preprint arXiv:1911.04488, 2019.
- [47] F. Kong, R. H. Stogner, D. R. Gaston, J. W. Peterson, C. J. Permann, A. E. Slaughter, R. C. Martineau, A general-purpose hierarchical mesh partitioning method with node balancing strategies for large-scale numerical simulations, in: 2018 IEEE/ACM 9th Workshop on Latest Advances in



Scalable Algorithms for Large-Scale Systems (scalA), IEEE, Dallas, TX, 2018, pp. 65–72.

- [48] B. Smith, P. Bjorstad, W. Gropp, Domain Decomposition: Parallel Multi-level Methods for Elliptic Partial Differential Equations, Cambridge University Press, Cambridge, United Kingdom, 2004.
- [49] A. Toselli, O. Widlund, Domain Decomposition Methods-Algorithms and Theory, Vol. 34, Springer Science & Business Media, Berlin, Germany, 2006.
- [50] X.-C. Cai, M. Sarkis, A restricted additive Schwarz preconditioner for general sparse linear systems, *SIAM Journal on Scientific Computing* 21 (2) (1999) 792–797.
- [51] F. Kong, Parallel memory-efficient all-at-once algorithms for the sparse matrix triple products in multigrid methods, arXiv preprint arXiv:1905.08423, 2019.
- [52] S. Kosaka, 3-D extension C5G7 MOX benchmark results using CHAPLET-3D, *Progress in Nuclear Energy* 48 (5) (2006) 439–444.
- [53] E. Lewis, M. Smith, N. Tsoulfanidis, G. Palmiotti, T. Taiwo, R. Blomquist, Benchmark specification for deterministic 2-D/3-D MOX fuel assembly transport calculations without spatial homogenization (C5G7 MOX), NEA/NSC 280.
- [54] J. W. Peterson, A. D. Lindsay, F. Kong, Overview of the incompressible Navier–Stokes simulation capabilities in the MOOSE framework, *Advances in Engineering Software* 119 (2018) 68–92.
- [55] B. S. Kirk, J. W. Peterson, R. H. Stogner, G. F. Carey, libMesh: A C++ Library for Parallel Adaptive Mesh Refinement/Coarsening Simulations, *Engineering with Computers* 22 (3–4) (2006) 237–254, <https://doi.org/10.1007/s00366-006-0049-3>.

- [56] A. Yamamoto, A. Giho, Y. Kato, T. Endo, GENESIS: a three-dimensional heterogeneous transport solver based on the legendre polynomial expansion of angular flux method, Nuclear Science and Engineering 186 (1) (2017) 1–22.